LA-UR-03-0371
December 2002

Advanced Accelerator Applications (AAA) Transmutation Science Progress Report: Fiscal Year 2002 Accomplishments

CONTENTS

ADVANCED ACCELERATOR APPLICATIONS (AAA) TRANSMUTATION SCIENCE PROGRESS REPORT: FISCAL YEAR 2002 ACCOMPLISHMENTS

Compiled by
Kemal O. Pasamehmetoglu
Los Alamos National Laboratory

December 2002

ABSTRACT

In this report, Fiscal Year 2002 (FY02) progress for the transmutation science research is summarized for the following six major categories:

1. Integration and Analytical Support
2. Materials research
3. Lead-Bismuth Eutectic (LBE) Research
4. Irradiation Experiments
5. High-Energy Physics Research
6. International Support

In FY02. the transmutation science activities also included Reactor Physics and Los Alamos National Laboratory (LANL) Sponsored University Research, which are not summarized in this report. The Reactor Physics work was primarily performed at Argonne National Laboratory (ANL) and summarized in related reports. Sponsored university research work is presented in the report summarizing the University Program.

The research tasks highlighted in this report are primarily conducted by LANL staff. In addition, ANL, Pacific Northwest National Laboratory (PNNL) and Oak-Ridge National Laboratory (ORNL) and Brookhaven national Laboratory (BNL) provided valuable technical support for these tasks. Finally, University of Michigan (UM) and University of Nevada - Las Vegas (UNLV) provided analyses and student support.

The FY02 tasks were defined to advance the proof-of-principle phase of the research program. This phase includes laboratory scale experiments and irradiation with relevant parametric conditions. The main objectives are to increase the confidence in the basic principles used to implement the transmutation science and to provide data for model validation and benchmarking.

In summary all the major research objectives for FY02 were met. As expected, some delays occurred in the interim progress, mostly caused by circumstances outside the control of the AAA program. However, none of those temporary delays impacted the long-term research objectives set forth for the transmutation science. Also, the transmutation science research to date has not shown any show stoppers for any of the implementation scenarios envisioned for the transmutation.

Major accomplishments in FY02 are listed below, while additional details and intermediate highlights are provided in the report.

- A ten-year research and development program plan is developed including a detailed cost-estimate for the transmutation scope defined under the AAA program.

- A high-temperature furnace is installed in the LANL hot-cell to perform high-temperature testing of irradiated structural materials.

- Revision 3 of the Materials Handbook was published including new chapters on LBE and 9Cr-1Mo alloy.

- The construction and commissioning of the DELTA loop for doing long-term corrosion and thermal-hydraulic testing with LBE was completed and the loop is approved for long-term unattended operations. This is the largest LBE loop in the U.S.A. and is equivalent in size and capabilities to other prominent loops in the world.

- Considerable progress was made in oxygen sensor and calibration technology and multiple probes are developed and calibrated for actual use in testing.

- An initial set of benchmark data for neutron yield and spectrum using LBE targets of varying diameter and with a 800-MeV proton beam were completed.

- The test apparatus for measuring helium and hydrogen production in structural materials was commissioned and the experimental process is validated. An initial set of data is obtained with iron samples.

- Multiple versions of the MCNPX were released to National and International users. These versions included various improvements for transmutation applications.

- A new and improved evaluation of Pu-239 and U-238 fission cross-sections up to 150 MeV neutron energies was completed.

- A new improved evaluation of the lead inelastic scattering cross-section was completed, with a potential impact of ~2.5% on reactivity predictions for lead-cooled systems.

- Considerable engineering, testing and physics assessment support was provided to MEGAPIE projects that has advanced to final design phase in FY02.

1. INTEGRATION AND ANALYTICAL SUPPORT

Objective:
The main objective of the Integration and Analytical Support task is to coordinate the Transmutation Science research over the various topical areas and in multiple institutions. Development and implementation of the research and development plan is the main task. Analytical support for the integrated implementation of the R&D plan is an essential part of the workscope.

Highlights:
The highlights for the FY02 Integration and Analytical Support activities are as follows:

- The final DRAFT of the 10-year R&D plan for the transmutation science was completed and submitted to DOE.
- A series of calorimetric experiments were performed to quantify the energy release during the mixing of sodium and LBE.
- A series of calculations to compare the waste stream from the two spallation target concepts—LBE and sodium-cooled tungsten were completed.
- Under the auspices of the DOE AAA Program, LANL hosted the Third International Workshop on Utilization and Reliability of High Power Proton Accelerators held May 12-17, 2002, in Santa Fe, New Mexico.

Major Tasks:
Short summary reports are provided for the followings tasks completed in FY02:

1.1. Transmutation Science Research and development plan
1.2. Lead-Bismuth Eutectic (LBE) - Sodium Compatibility Experiments
1.3. Product Inventory for LBE and Sodium-Cooled Tungsten Targets
1.4. OECD Accelerator Reliability and Utilization Workshop
1.5. Analytic Support for the LBE Target Neutron Yield Experiments

In addition, the following were other activities performed under this program element:

- Multiple presentations to the internal and external review committees;
- Participation in International Collaboration meetings and related presentations;
- Management of the work-packages for budget, scope and schedule; and
- Preparation of FY03 planning packages.

1.1. Transmutation Science Research and Development Plan

Objective:
The objective of this plan was to lay out the research and development needs for 10-years leading up to the proof-of-performance phase for a transmuter.

Accomplishments:
The 10 year R&D plan for transmutation science was completed using the technology readiness level (TRL) concept developed by NASA. It was submitted to DOE as a FINAL DRAFT. The contents were included in the AAA Transmutation Technology Development Plan (LA-UR-02-5312).

The transmutation science development plan presents the research and development (R&D) plan for the transmutation physics, spallation targets, materials and coolants portion of the accelerator driven transmutation program. The plan covers the proof-of-principle phase of the research program spanning from FY01 through FY10. The planned research is divided into four general categories. The general categories and the major issues covered under each category are as follows:

Transmutation Physics:
- Improvements, benchmarks, verification and validation of radiation transport and burnup codes used to simulate transmuter performance.
- Cross-section measurements and evaluations up from 1 keV to 150 MeV neutron energies.

Materials:
- Structural and physical properties of materials exposed up to 100 dpa and helium-to-dpa ratios ranging from 1 to 160 appm/dpa.
- Thermal fatigue limits.
- Maintenance of an International Materials Handbook.
- Development of structural design criteria.

Lead-Bismuth Eutectic Technology:
- Liquid metal corrosion and corrosion control strategies.
- Thermal-hydraulics performance.
- Instrumentation development.
- Chemical thermodynamics (impact of spallation and impurities).
- Liquid-metal embrittlement (with and without radiation).

Target technologies:
- Compatibility of target and multiplier coolants.
- Decision on solid versus liquid target options.
- Biological dose-conversion factors for the spallation and activation products.

The main research objectives of the proof-of-principle phase are as follows:
- ¥ Verification and validation of the radiation transport codes via the use of separate effect and integral effect experiments such that technology selection studies can be based on accurate simulations;
- ¥ The development of the performance envelope for the materials and the coolants including achievable flux and fluence limits and limits on thermodynamic and thermal-hydraulic parameters; and

- Demonstration of the spallation target operations with the essential support systems at ~1-MW beam power.

To achieve these objectives, the resolution strategy includes both experimental and analytical studies. However, the strategy relies heavily on separate-effect and integral effect experiments. In general, the required experimental facilities exist to complete the proof-of-principle phase of the research. However, one essential facility, which is a test station at the end of the LANSCE beam, requires major upgrades and improvements. This facility must be available by 2006 to achieve the stated research objectives. The research roadmap in terms of the experimental facilities needed to complete the proof-of-principle, and leading up to the initiation of proof-of-performance in an Accelerator Driven Test Facility (ADTF) by ~FY2010 is summarized in the Fig. 1.1-1.

Within the next 8 years, some critical decisions must be made for a successful and timely implementation of this program.

- The first decision must come within the next 2-3 years on development and construction of the test facility to be used for proof-of-performance subsequently leading to a demonstration facility.

- The second decision that must be made is on the choice of technologies such as ADS versus low-conversion-ratio fast reactors, fuel types, etc Within the proposed plan, the technical data generated will be adequate to make that decision within 5 to 6 years starting with FY03.

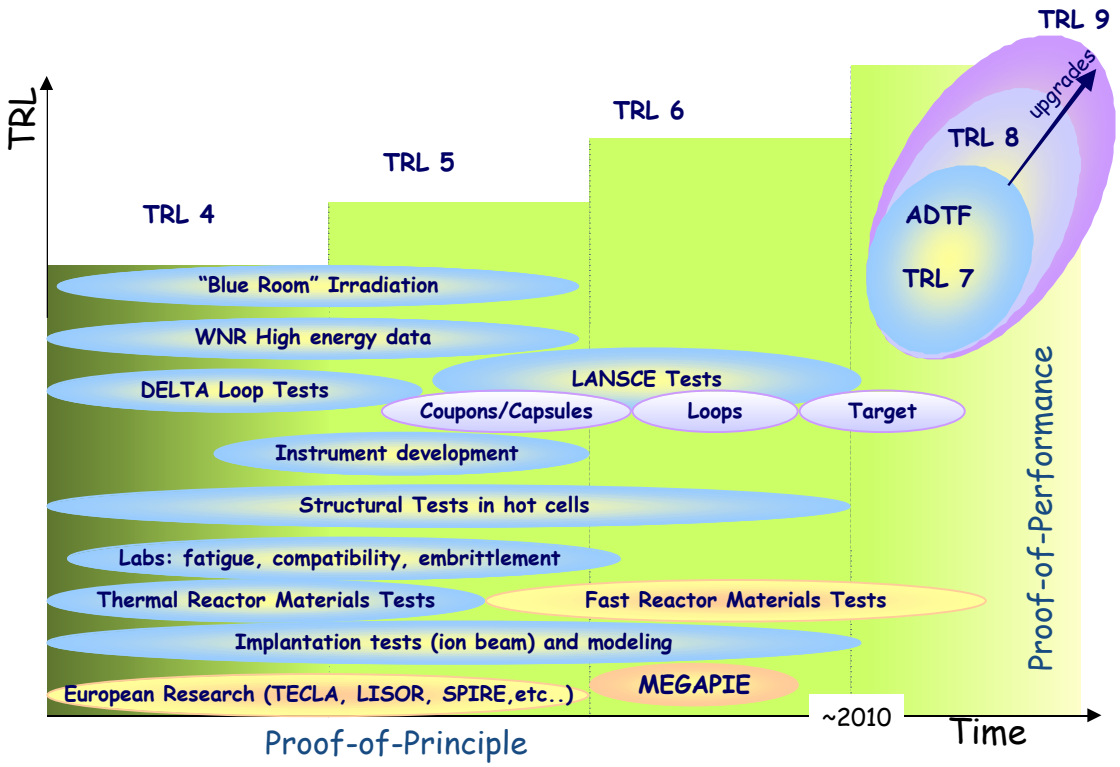

Fig. 1.1-1: Summary of R&D activities for transmutation science.

An initial estimate for the budget required to achieve the stated research objectives also is provided in the plan. In developing the budget estimate, considerable credit is taken for the ongoing International collaborations with the French CEA and the MEGAPIE initiative in Europe. Additional collaboration opportunities also exist, which may result in further savings in the upcoming years. The budget estimate, shown in Fig. 1.1-2, also includes considerable funding for university participation in the programmatic research.

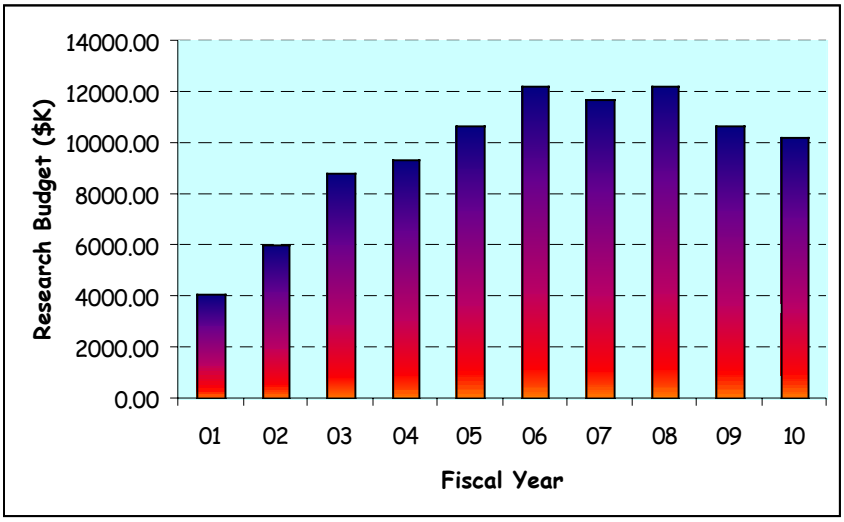

Fig. 1.1-2: Projected 10-year budget profile for transmutation science.

Conclusions:
The direction was changed at the end of FY02 as the program transitioned from AAA to AFCI with less emphasis on Accelerator Driven Systems. Thus, the R&D plan requires revision in FY03. A large fraction of the material in the current plan can be used to develop the new plan under the AFCI program.

For additional information contact Kemal Pasamehmetoglu (LANL), at kop@lanl.gov.

1.2. Lead-Bismuth Eutectic (LBE) - Sodium Compatibility Experiments

Objective:
For transmutation scenarios in which an LBE target is used inside a sodium-cooled sub-critical blanket, the compatibility of the two coolants are of interest. A less likely scenario in which the two fluids may be used together is when a sodium-bounded fuel is deployed inside an LBE-cooled blanket. The objective of this task was to complete a series of calorimetric experiments (started in late FY01) to investigate the thermal energy and reaction product yields when sodium is mixed with lead, bismuth, and LBE.

Accomplishments:
A series of calorimetric experiments are run to investigate the mixing of sodium with lead, bismuth and LBE. The experimental setup is shown in Fig.1.2-1. A small volume of lead, bismuth, or LBE is contained above the mixing chamber filled with sodium. A diaphragm is ruptured to inject the lead, bismuth, or LBE into the sodium. For fast injection tests, the puncture area is ~2 cm^2. A smaller size lance is used for the slow injection tests when the puncture area is ~ 2 mm^2. The mixture temperature is recorded by thermocouples. For selected tests, samples are obtained for analyzing reaction products. The test matrix is shown in Table 1.2-1, along with the peak temperature results for the completed tests. Typical temperature traces are shown in Fig. 1.2-2.

The temperature spikes typically occur near the bottom of the mixing chamber. One unexpected result was that the temperature spike for the only slow injection test was larger than the equivalent fast injection tests. However, one must remember that those are obtained by discrete thermocouples, and it is difficult to assume that the initial reaction always occurs where the thermocouple is located. Examination of the post-test mixtures indicated the gritty texture of the reacted Na. The product did not form large particles at any of the temperatures or˚at either injection rate, but rather formed a very fine submicron-sized particulate that explains the grittiness.

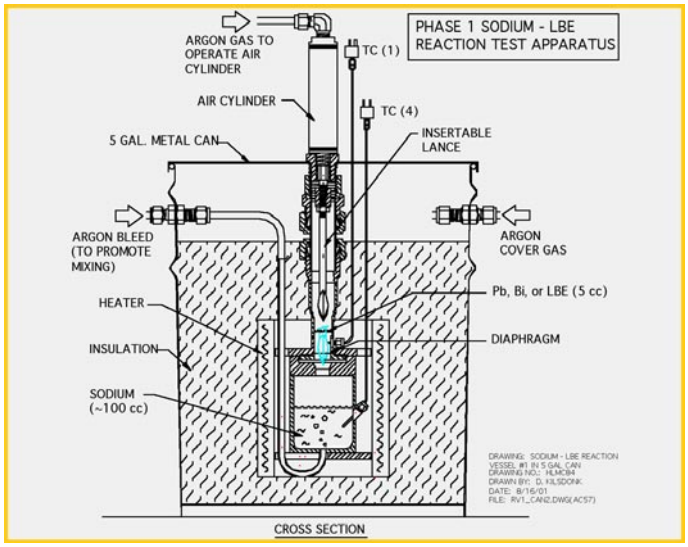

Fig. 1.2-1: Experimental setup for the LBE-sodium compatibility tests.

Conclusions:
The scoping experiments showed that when sodium is mixed with LBE, there is an exothermic reaction. Some of the reaction products form a high-meting point solid resulting in a gritty structure in the mixture. Based on these results, for transmuter designs where sodium and LBE are used together, the accidental mixing scenarios must be carefully considered. Additional testing under more realistic mixing scenarios may be required to properly quantify the consequences of such incidents.

For additional information, please contact John Holland (ANL), at jwholland@anl.gov.

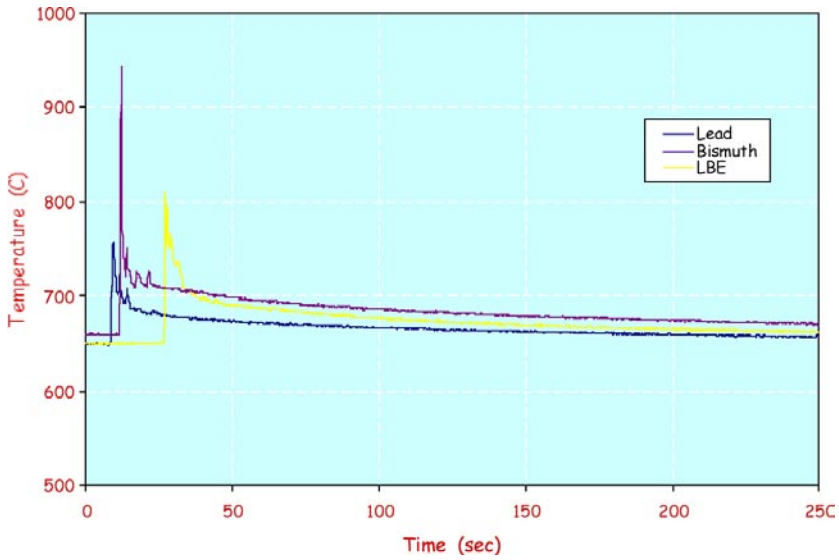

Fig. 1.2-2: Temperature traces for the 600¡C mixing tests.

Table 1.2-1: Test Matrix for LBE-Na Compatibility Experiments

Test Date (YMD)	Initial Temp (°C)	Injection Speed (Area)	Sodium Volume (cm^3)	Heavy Metal		Max. Temp Increase (°C)
				Injection Material	Volume (cm^3)	
011023	600	Fast (2 cm^2)	50	Pb	2.5	110
011026	600	Fast (2 cm^2)	50	Bi	2.5	285
011102	600	Fast (2 cm^2)	50	LBE	2.5	165
020208	600	Slow (2 mm^2)	50	LBE	2.5	150
011018	400	Fast (2 cm^2)	50	Pb	2.5	115
020215	400	Fast (2 cm^2)	50	Bi	2.5	225
020212	400	Fast (2 cm^2)	50	LBE	2.5	235
011120	400	Slow (2 mm^2)	50	LBE	2.5	310
011115	200	Fast (2 cm^2)	50	LBE	2.5	60
020206	200	Slow (2 mm^2)	50	LBE	2.5	20

1.3. Product Inventory for LBE and Sodium-Cooled Tungsten Targets

Objective:
The objective was to perform some initial calculations for a typical LBE and sodium-cooled tungsten targets in order to assess the reaction product inventory for toxicity comparisons.

Accomplishments:
A set of calculations to compare the waste stream from the 2 target concepts—LBE and sodium (Na)-cooled tungsten was completed. For this comparison, a nine-month irradiation of the targets using a 600-MeV, 15-mA proton beam was assumed. Within the target region there is either 510 kg of tungsten with 25 kg of Na (50% tungsten volume fraction) or 540 kg of LBE. The total loop volume is not used for the coolant for simplicity. The secondary reactions are negligible and the final radioactive material inventory is nearly independent of the total coolant volume. The final results are shown in Fig. 1.3-1 for the total activity and for the ratio to Category III limits, used as a measure of the toxicity. Note that not all reaction products have dose conversion factors available. Those products, typically with low activity, are ignored but may have an effect on radiotoxicity. Figure 1.3-1 shows that total activity of the Na-cooled target is higher than the LBE target during the first ~3000 days of cool-down, primarily due to tungsten isotopes (e.g. W-187). However, LBE is more toxic than the Na-cooled target during the first ~1000 days, because of Polonium (Po) -210 production in the LBE system. In this study, we used a beryllium reflector on one side of the target, resulting in a large thermal neutron population. Consequently, Po production is larger than one would get in a truly fast system.

Conclusions:
These results can be used only for an order of magnitude estimate indicating that there is not much difference between the two targets in terms of the waste stream.

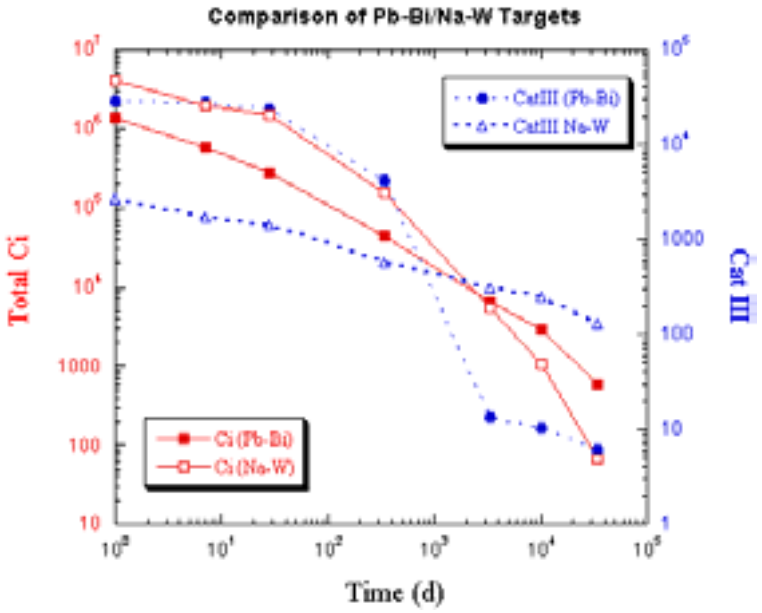

Fig. 1.3-1: Reaction products comparison for the LBE and Na-cooled tungsten targets.

For additional information, please contact Mike James (LANL), at mrjames@lanl.gov.

1.4. OECD Accelerator Utilization and Reliability of High-Powered Proton Accelerators Workshop

Objective:
Accelerator Utilization and Reliability Subgroup (AURS) of the within OECD (Organization for Economic Cooperation and Development)/Nuclear Energy Agency (NEA) Working Party on Partitioning and Transmutation (WPPT) is one of the four subgroups tasked with determining the viability of spent fuel partitioning and transmutation. The objective of the workshop was to discuss the research status and R&D needs for the utilization of the high-powered proton accelerators for transmutation of spent nuclear fuel.

Accomplishments:
LANL hosted the Third International Workshop on Utilization and Reliability of High Power Proton Accelerators held May 12-17, 2002, in Santa Fe, New Mexico.

The workshop included 9 invited talks and 22 contributed papers covering the following topics:

- Reliability of the accelerator and impact of beam interrupts on the design and performance of the ADS.
- Spallation target design characteristics and impact on the multiplier design (Materials, radiation damage and embrittlement; enhanced corrosion; cooling issues with high-power density; and windowless design concepts)
- Safety and operational characteristics of a sub-critical system driven by a spallation source.

The papers were balanced among various topics covered by the workshop. Accelerator technology papers comprised 28% of the workshop; the spallation target technology comprised 36%, and the remaining papers addressed the operational and safety issues (27%) and test facilities (9%). Also, there were four group discussions: accelerator technology, target technology, multiplier and coupling issues, and safety issues.

Conclusions:
The workshop provided a very useful forum for reviewing the International research status and discussing the future needs for additional research. The discussions resulted in identifying the need for International expert groups to address the following two topics:

- International database on accelerator reliability and extrapolation to today s technology

- LBE handbook development based on International experiments and analyses.

The proceedings of the workshop along with the findings of the group discussions will be published as an OECD (Organization for Economic Cooperation and Development) report.

For additional information contact Kemal Pasamehmetoglu (LANL), at kop@lanl.gov.

1.5 Scoping Calculation for the Neutron Yield Experiments

Objective:
The objective of this task was to help in the design of the LBE neutron yield experiments. The location of the activation foils, the expected yield, and geometric design issues were within the scope of the analytical support task.

Accomplishments:
A number of scoping calculations using MCNPX (merged code that˚includes both Los Alamos High-Energy Transport (LAHET) and Monte Carlo N-Particle (MCNP) codes) to assess the data quality in the LBE target neutron yield experiments were performed The impact of the support structure on the activation foil measurements of flux was small, but the effect was not negligible. The estimated impact from the aluminum support plate was to increase the lower surface flux by ~10%. Foils were placed around the target at the 10-cm location to compare symmetry effects. The calculated neutron flux intensity around the target is shown in Fig. 1.5-1. The expected count rates at the detectors down the flight paths were also calculated with MCNPX (Fig. 1.5-2) to determine what, if any, changes needed to be made on the collimator configuration. It was determined that the count rates were not excessive, and the existing configuration was used in the experiment.

Much progress was made in analysis of the neutron yield from the thick Pb-Bi target. The counting of the 14 stacks of activation foils was completed, with many of the significant foils counted more than once to verify isotopes with decay information. Most of the counting in this period was performed to sample the longer-lived isotopes. The beam history data for the Blue Room irradiation and the Target-4 irradiation were assembled to create the production histories of the isotopes from their measured activities using the BCF program. The group of foils placed in Target-4 were analyzed with STAYSL and compared to the known spectrum in that location (Fig. 1.5-3). Based on those initial results, a best fit spectrum was determined based on the isotopic results that fit the known spectrum extremely well.

As part of this process, numerous evaluations and additions of cross-section data have also been made to the STAYSL package, including additions of Bi and Tb (n,xn) reactions.

Coclusions:
The detailed etst plan based on pre-test analyses led to succesful execusion of two series of tests with 2 different target diameters. The test results are discussed in section 4.1.

For additional information, please contact Mike James (LANL), at mrjames@lanl.gov .

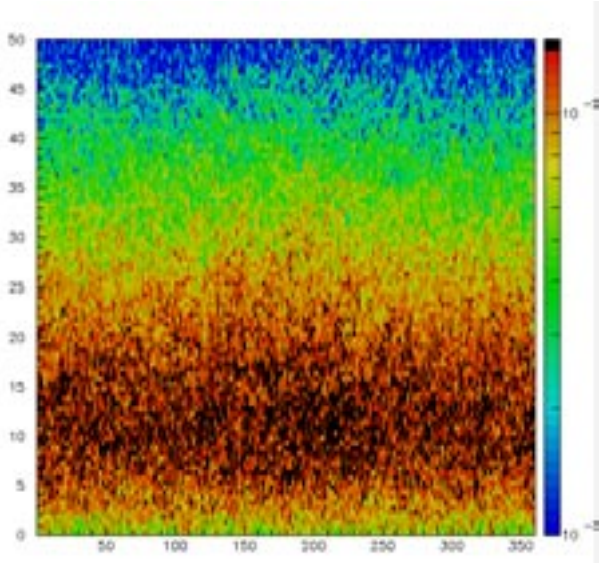

Fig. 1.5-1: Image of surface flux of Pb-Bi target. (X axis is in degrees, y axis is in position along target. Color denotes neutron flux intensity).

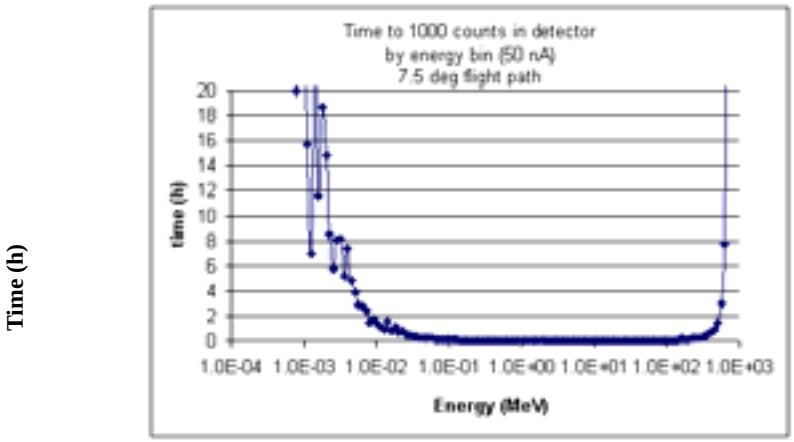

Fig. 1.5-2: Time necessary to get sufficient counts for adequate statistics.

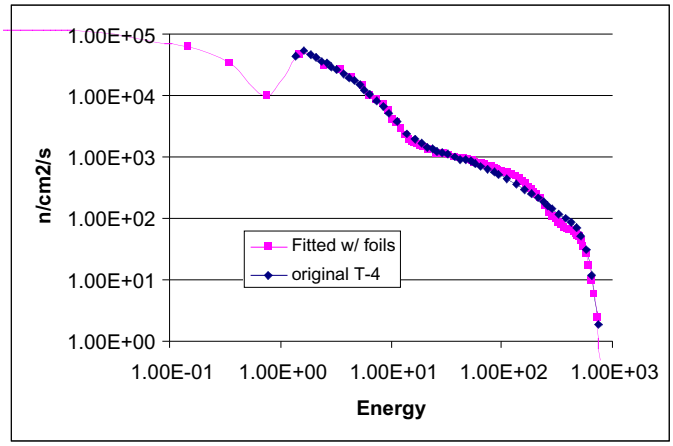

Fig. 1.5-3: Preliminary results of Target-4 foil analysis.

2. MATERIALS RESEARCH

Objective:
The overall objective of the materials research is to quantify the effect of radiation damage (under proton and neutron irradiation) on material properties. The main property of interest is the material ductility as a function of displacement per atom (dpa) and gas production (helium and hydrogen) caused by irradiation over a wide range of energy spectrum of interest. The results are included in the Materials Handbook that can support the fast spectrum transmuter design.

Highlights:
The following are the major accomplishments in FY02 for the Materials Research activities:

- In order to understand the elevated-temperature tensile behavior, TEM analysis on the irradiated 9Cr-1Mo and SS-316L samples was performed.
- Shear-punch testing on irradiated SS-316L samples were completed and the results are used to predict the tensile properties.
- High temperature testing of 9Cr-1Mo samples (irradiated at low temperature) was completed.
- A high-temperature furnace was installed at LANL hot-cell.
- An extensive review of HT-9 for Ads applications was completed. Also, ion-beam implanted HT-9 samples were analyzed for radiation behavior.
- Compression testing on tungsten samples manufactured by different techniques were completed at various temperatures.
- Revision 3 of the AAA Materials Handbook was published with two new chapters (9Cr-1Mo, LBE) and revisions on 4 existing chapter (Tungsten, SS-316L, Alloy 718, Al-6061-T4).

Major Tasks:
Short summary reports are provided for the following tasks completed in FY02:

2.1. Transmission Electron Microscopy on 9Cr-1Mo and SS-316L Samples
2.2. Shear-Punch Testing of SS-316L Samples
2.3. High-Temperature Testing of Structural Materials
2.4. Cladding and Duct Review for HT-9
2.5. Proton Irradiation of HT-9
2.6. Tungsten Compression Testing
2.7. AAA Materials Handbook

In addition, considerable hot-cell clean-up activities were conducted in FY02. Irradiated samples were shipped from PNNL and ORNL to LANL, where they were stored.

2.1. Transmission Electron Microscopy on 9Cr-1Mo and SS-316L Samples

Objective:
The objective is to perform TEM analysis on the irradiated 9Cr-1Mo and SS-316L samples in order to understand the elevated-temperature tensile behavior.

Accomplishments:
TEM Analyses of Irradiated Steel Samples at PSI
Transmission Electron Microscopy (TEM) was performed on Mod 9Cr-1Mo that had been irradiated to 1.4 dpa at 35-70¡C and subsequently thermally aged at 500¡C for about 2 hours. Observations reveal no bubble formation. Figure 2.1-1 shows a TEM image of a thermally aged (500…C) 1.4-dpa specimen next to a 9-dpa specimen with no thermal aging. Estimated He and H content in these samples were estimated to be 87 appm and 737 appm, respectively. It was thought that thermal aging at 500¡C may lead to the formation of small gas-filled bubbles or cause the coarsening of black spot (interstitial loop) damage that may be present. Initial observations showed no evidence of any cavities (however, note that the maximum observable cavity size in TEM is ~1.5 nm). A second set of observations to examine the black-spot morphology. Due to oxidation of the sample surfaces and due to the highly magnetic character of Mod 9Cr-1Mo, it was not possible to make any clear observations of black-spot damage.

For additional information, please contact Mychailo Toloczko (PNNL), at mychailo.toloczko@pnl.gov .

TEM Analyses of Irradiated Steel Samples at PSI
Analysis was performed on SS-316L at PSI after irradiation in the SINQ accelerator by LANL staff located at PSI. Microstructures of materials were studied after exposure to an environment of high-energy protons plus spallation neutrons. The material studied received a maximum total charge of 6.8 Ah of protons with a peak fluence of 3.2×10^{25} p/m^2, which correlates to a dose between 2.5 and 9.7 dpa. The temperature range for the specimens studied was between 70¡C and 300…C. As shown in Table 2.1-1 and Fig. 2.1-2, the mean size of Frank loops grew with increasing dose while the density remained constant. The density and mean size of small-defect clusters and stacking-fault tetrahedral (SFT) remained relatively constant with increasing dose. These results show a good agreement with previous measurements.

For additional information, please contact Rob Rutherford (LANL) at rwr@lanl.gov .

Conclusions:
TEM analyses performed on low-dose samples were inconclusive in terms of understanding the tensile behavior of irradiated 9cr-1Mo at elevated temperatures. The defect density and size data for the SS316L samples provide valuable data for basic modeling studies to understand the effect of radiation damage on materials properties.

Table 2.2-1: Dose Dependent Irradiation Defects in SS-316L, Including Small-Defect Clusters, Frank Loops, and Stacking-Fault Tetrahedral (SFT)

Dose (dpa)	Irradiation Temperature (C)	Small Cluster		Frank Loop		SFT	
		mean size (nm)	density (m^3)	mean size (nm)	density (m^3)	mean size (nm)	density (m^3)
2.5	74-87	1.6	3.7×10^{23}	6.5	9.8×10^{22}	1.5	5.6×10^{22}
5.8	188-222	1.6	4.0×10^{23}	14.1	6.9×10^{22}	1.5	4.0×10^{22}
9.7	262-305	1.7	4.1×10^{23}	17.4	6.0×10^{22}	1.5	6.5×10^{22}

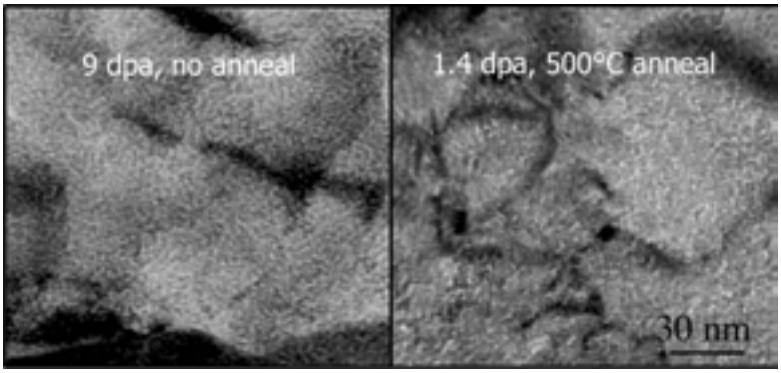

Fig. 2.1-1: TEM image showing no bubble formation after 500¡C anneal.

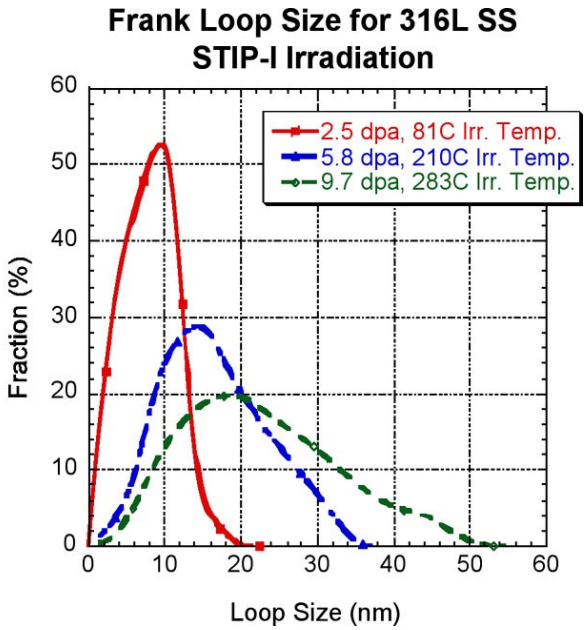

Fig. 2.1-2: Effect of dose on fractional percent of Frank loop size.

2.2. Shear-Punch Testing of SS316L Samples

Objective:
The objective is to perform shear-punch tests were on unirradiated and irradiated SS-316L as a way to extend the number of specimens available for estimation of tensile properties.

Accomplishments:
Shear punch tests have been performed at 300¡C on SS-316L irradiated to 9.7 dpa and 1.7 dpa. These results are compared to results from tensile tests performed on SS316L irradiated to similar doses. The shear-punch tests traces are shown in Fig. 2.2-1. With excellent reproducibility, the tests show an increase in yield strength, a more sharply defined yield point, and an increase in ultimate shear strength with increasing dose. As expected from examination of the test traces, shear yield and shear ultimate strength both increase with increasing dose. Using previously derived linear correlations between shear-punch test properties and uniaxial tensile properties, uniaxial yield strength, uniaxial ultimate strength, and true uniform elongation were estimated from the shear-punch properties and are shown in Fig. 2.2-2 along with actual measured tensile properties obtained from tensile tests at 300¡C on unirradiated SS316L specimens and SS316L specimens irradiated to 2.5 dpa. As the specimens were irradiated near room temperature, the estimated tensile properties support the idea that tensile test temperature has a strong effect on tensile properties of SS316L at these moderate mechanical property test temperatures. The correlations used for estimation of tensile properties from shear punch properties were derived from a series of shear-punch tests and tensile tests performed on a variety of unirradiated materials.

Conclusions:
The predicted tensile properties from shear-punch tests are in generally good agreement with the observed tensile properties at 0 dpa and 2.5 dpa. The shear-punch tests predict that after 10 dpa at 35¡-67¡C, the uniaxial yield strength will be approximately equal to the uniaxial ultimate strength, and the uniform elongation will drop to approximately zero. These predicted tensile properties at 300¡C are similar to the available data in the open literature on tensile properties of SS-316L irradiated and tensile tested near 300¡C.

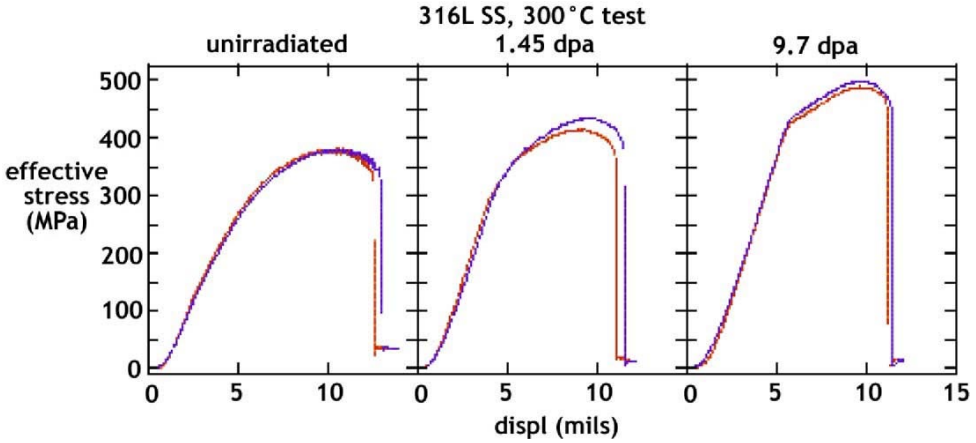

Fig. 2.2-1: Effective shear stress vs. crosshead displacement traces of shear punch tests performed at 300¡C on SS-316L.

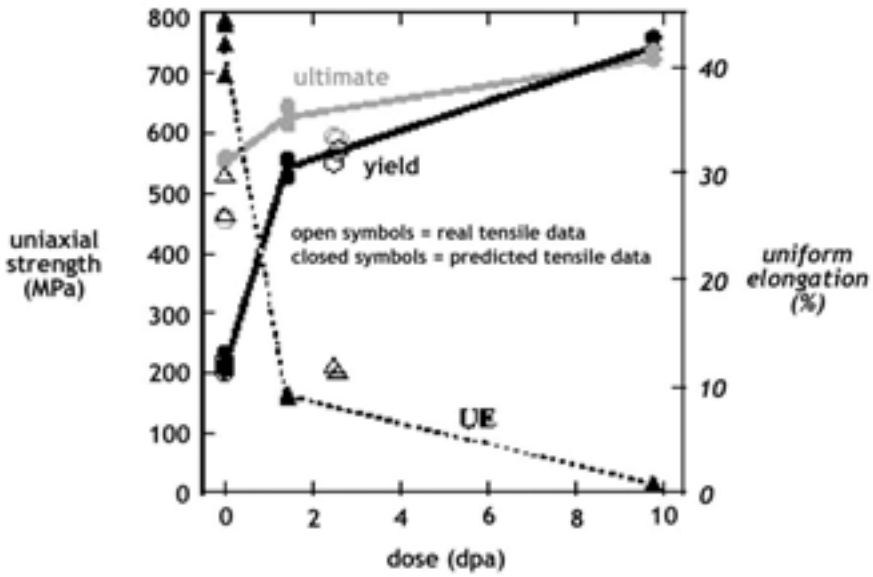

Fig. 2.2-2: Observed tensile properties and tensile properties predicted from shear punch tests for tests performed at 300¡C on SS-316L.

For additional information, please contact Mychailo Toloczko (PNNL), at mychailo.toloczko@pnl.gov.

2.3. High-Temperature Testing of Structural Materials

Objective:
The objective is to test the irradiated structural material samples at different temperature that are relevant to transmutation applications. Currently, the samples irradiated at low temperatures († 160¡C) in previous irradiation campaigns are being tested.

Accomplishments:
PNNL Tests on 9Cr-1Mo Samples
One irradiated and two unirradiated tensile tests were performed up to 600…C on Mod9Cr-1Mo (T91). Results plotted in Fig. 2.3-1 show, at elevataed temperatures, little difference when compared to unirradiated data. A report that summarizes the tensile properties of candidate AAA structural materials was revised to include the new data.

For additional information, please contact Mychailo Toloczko (PNNL), at mychailo.toloczko@pnl.gov .

High-Temperature Furnace
A high temperature furnace designed by MRF furnaces was set-up, tested (up to 700¡C in argon), then installed in a hot cell with cooling lines, thermocouples and power leads routed through the hot-cell wall. The hot-cell is located at the Chemistry and Materials Research (CMR) Building at LANL.

For additional information, please contact Stuart Maloy (LANL) at maloy@lanl.gov .

Conclusions:
The testing done on 9Cr-1Mo samples with irradiation up to 3 dpa show that at temperatures ‡ 400¡C, the tensile properties recover those that correspond to unirradiated samples, indicating considerable annealing effects. The furnace installed in the LANL hot cell will be used for doing similar tests in the future.

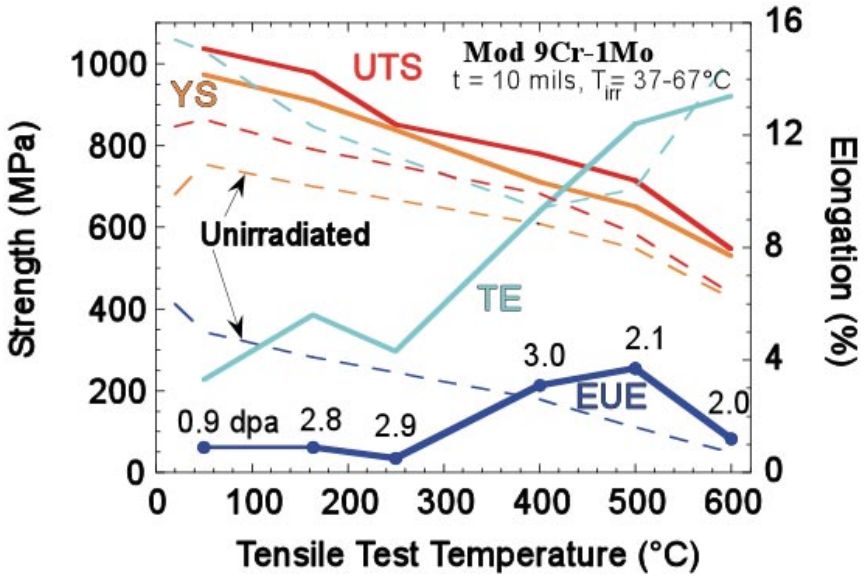

Fig. 2.3-1: Mechanical properties of Mod 9Cr-1Mo after irradiation in a proton beam at 37…C to 67…C and tested at temperatures from 50…C to 600…C.

2.4. Cladding and Duct Review for HT-9

Objective:
The objective was to complete and document a review of the available data and studies on HT-9 for applications in the AAA program.

Accomplishments:
A report, Advanced Accelerator Applications Cladding and Duct Review, was issued by ANL-West. Based on the performance of HT-9 in the fast reactor program and the fusion energy program, the following initial conclusions and recommendations have been reached for fuel and cladding applications for ADS systems:

1) In the temperature range of 400¡C—650¡C, HT-9 has adequate swelling resistance, toughness, strength, and ductility.

2) At room temperature, HT-9 that has been irradiated at lower temperatures (conservatively <400¡C) can become brittle and hot cell operations must ensure no excessive stress is placed on cladding and duct material. Notches or stress concentrations in the design must be avoided.

3) Because of the high ductile-to-brittle transition temperature (DBTT) measured in material irradiated in the High Flux Isotope Reactor (HFIR) at 400¡C, which had He concentrations of 353-391 appm, He limits should be applied to HT-9 used in ADS cladding and ducts until prototypical experimental data can be obtained. Also, a minimum irradiation and minimum handling temperature for irradiated HT-9 components should be set.

4) Because of large amounts of hydrogen and helium generated in ADS materials, a test program to determine the synergistic effects of He and H on mechanical performance should be undertaken. A test facility producing a prototypical spallation neutron spectrum would be ideal.

5) A test program needs to be continued to better understand the interaction between fuel and HT-9 cladding. Until the mechanisms of interaction are understood, a transient limit of 725¡C should be placed on the cladding inner surface.

6) Alloys are under development that may improve performance relative to HT-9. Programs aim to improve high temperature creep strength and low temperature toughness. A component of the ADS program should study the performance of these promising alloys systems.

Conclusions:
The review shows that HT-9 is a promising material for ADS applications but further testing is necessary to take full advantage of its properties. Especially, the new HT-9-based alloys that are being developed can be quite promising for ADS applications.

For further information, please contact Todd Allen (ANL-W) at todd.allen@anlw.anl.gov .

2.5. Proton Irradiation of HT-9

Objective:
The objective is to perform the microstructural characterization of the irradiated HT-9. The materials were irradiated with 2.0 MeV protons at an irradiation temperature of 450…C to doses of 3, 7 and 10 dpa (either with or without He-implantation of 100 appm).

Accomplishments:
The profile of He distribution along with the displacement damage of 2 MeV protons in HT-9 is shown in Fig. 2.5-1. The irradiated HT-9 coupon has a geometry of 2x20x0.5 mm as a rectangular bar. Due to the narrow width of the He implantation, the thin area of the foil for microstructure examination should be controlled to a depth of 2-3 μm below the irradiated surface. The sample preparation has proven successful in cutting down a magnetic field interference with the electron beam in the electron microscope.

Two TEM samples were prepared, one with and one without He-implantation, both irradiated to a dose of 3 dpa. The overall microstructure for the He-implanted sample irradiated to 3 dpa at 450…C is very similar to the unirradiated HT-9 except the presence of dislocation loops. The sample consisted of low-density dislocation loops, high-density dislocations, dislocation cell boundaries, precipitates, and lath structure. No voids were found. The dense dislocation structure in the irradiated HT-9 is similar to that in the unirradiated HT-9, shown in Fig. 2.5-2. The irradiation-created dislocation loops in HT-9 are shown in Fig. 2.5-3 under three different diffraction conditions. The average loop size is 10.8 nm with a number density of 1.2×10^{21} m^{-3}. The precipitate structure in the irradiated HT-9 (3 dpa at 450…C, He-implanted) is similar to that in the unirradiated HT-9. No irradiation-induced phases were identified. The analysis of diffraction spots and x-rays from the precipitates revealed that the precipitates have an FCC structure with a lattice constant about 1.09 nm and a composition in atomic fraction of 29%Fe +64%Cr +3.9%Mo +1.3%V and 0.8%W. This is in close match to $M_{23}C_6$. Figure 2.5-4 shows the images of precipitates under both bright field and dark field imaging conditions.

Comparing the result to the Gelles and Kohyama reference[1], voids were not found in HT-9 irradiated in EBR-II to 70 dpa in the temperature range of 400…C—450…C, although helium bubbles were formed at temperatures as low as 400…C. The result from the proton irradiated HT-9 is consistent with neutron result. Although the implantation of 100 appm He may assist the void development, the dose of 3 dpa may be still too low to form the cavity. The dislocation loops examined in the work by Gelles were also identified as a<100> type. The type of the loops identified in the proton irradiated HT-9 is also in agreement with the reference.

Conclusions:
The analyses and the results show that displacement damage and helium implantation studies by using ion-beams can provide a valuable tool in the fundamental understanding of the radiation damage on structural materials. These techniques can be used to interpolate extrapolate the existing data to data regimes where extensive high-energy neutron irradiation data is not available.

[1] D. S. Gelles and Akira Kohyama, DOE/ER-0313/6, 1989

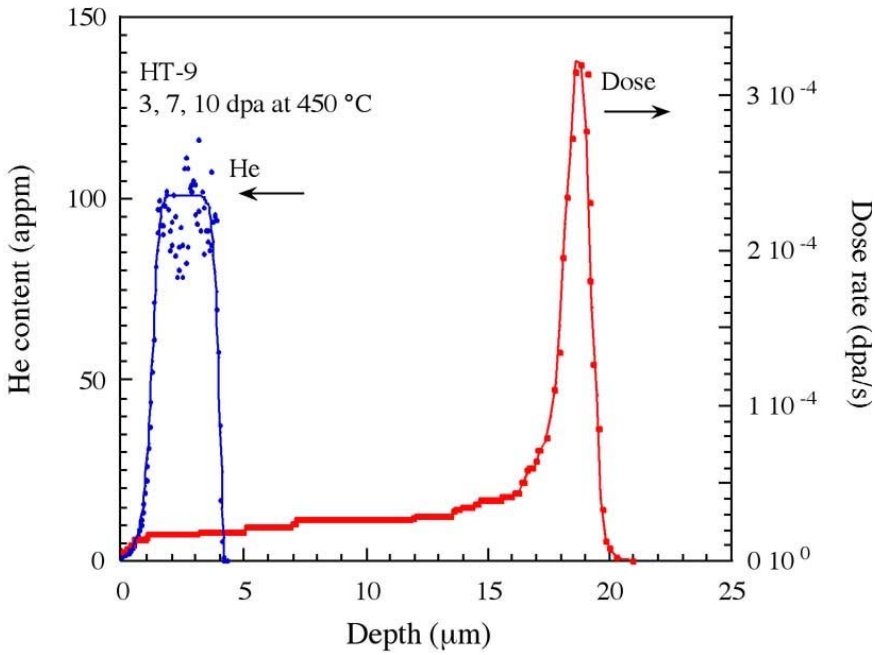

Fig. 2.5-1: He distribution profile and the 2 MeV proton damage profile for HT-9 irradiated with protons to doses of 3, 7 and 10 dpa at 450…C.

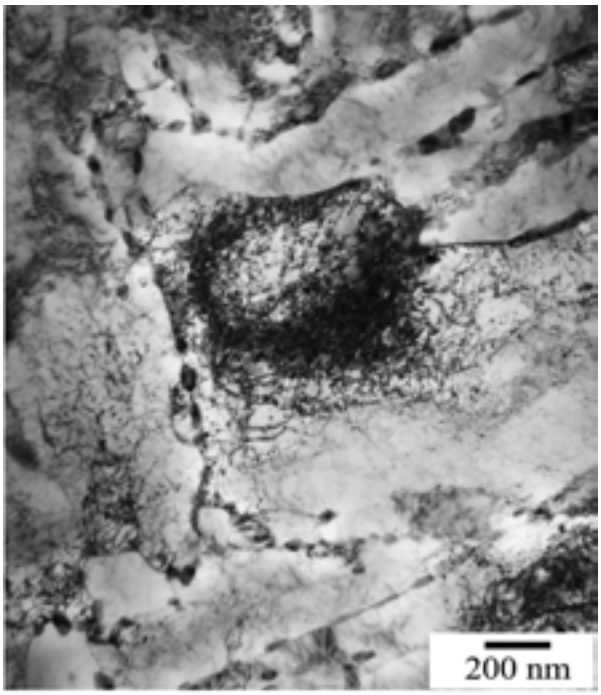

Fig. 2.5-2: Overview of the microstructure for HT-9 implanted with 100 appm He followed by proton irradiation at 450…C to a dose of 3 dpa.

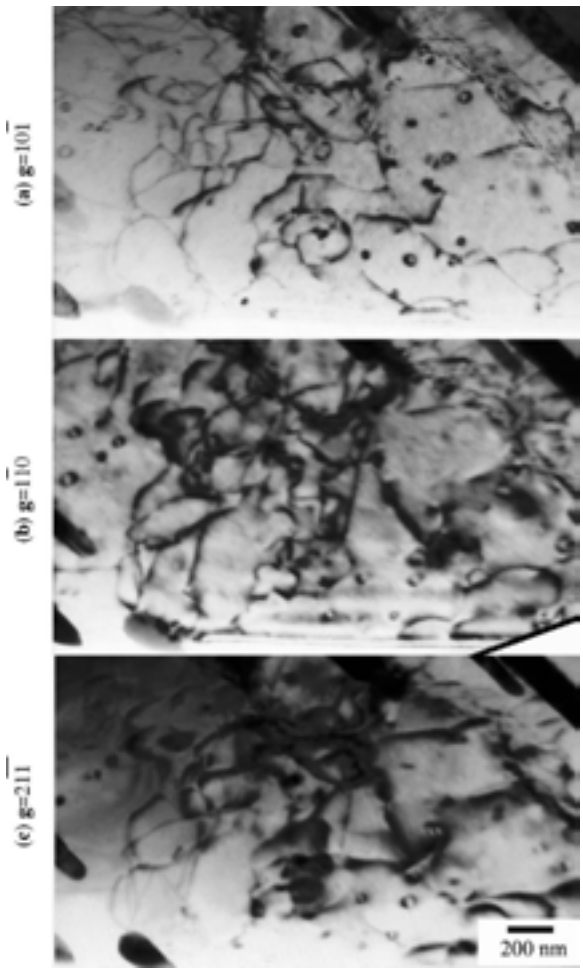

Fig. 2.5-3: Dislocation loops in HT-9 implanted with 100 appm He followed by proton irradiation at 450…C to a dose of 3 dpa.

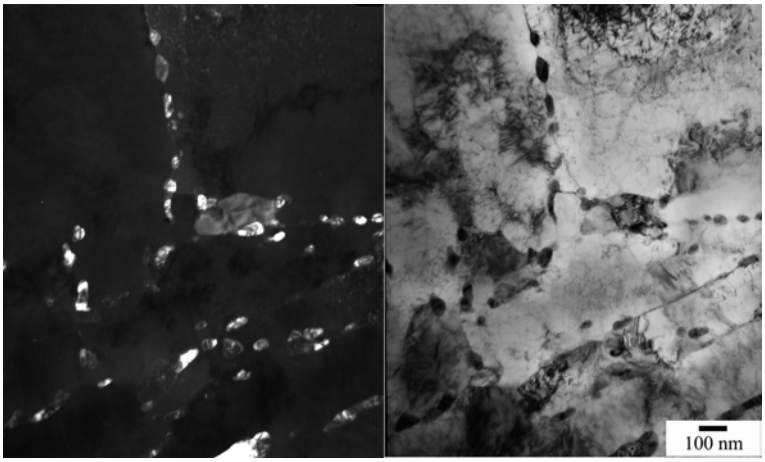

Fig. 2.5-4: Images of precipitates in HT-9 implanted with 100 appm He and irradiated with protons at 450…C to a dose of 3 dpa.

For further information, please contact Todd Allen (ANL-W) at todd.allen@anlw.anl.gov .

2.6 Tungsten Compression Testing

Objective:
The objective was to obtain compression data on tungsten samples obtained using different manufacturing techniques at different temperatures.

Accomplishments:
Compression testing of tungsten was conducted to 20% plastic strain using a strain rate of 10^{-3} at temperatures of 25°C, 150°C, and 300°C. Testing was performed on the tungsten manufactured in the following ways:

- Drawn wrought tungsten,
- Drawn wrought tungsten/annealed at 1800°C for 15 hours,
- Vapor plasma spray (VPS),
- Chemical vapor deposition (CVD) tested parallel to growth direction; and
- CVD perpendicular to the growth direction (axial).

The results are shown in Figs.˚2.6-1 and 2.6-2. Wrought tungsten tested in compression had a yield strength of ~1150 MPa, ~750˚MPa, and ~425 MPa when tested at 25¡C, 150¡C, and 300°C, respectively. Although the decrease in percent yield strength from increasing temperature varied between the different types of processed tungsten, all forms exhibited a substantial decrease in yield strength with increasing temperature. Wrought tungsten exhibited the highest yield strength of ~1150 MPa, followed by VPS˚at ~800 MPa. CVD axial showed a yield strength of ~750 MPa. CVD radial and annealed tungsten both revealed a yield strength of ~600 MPa.

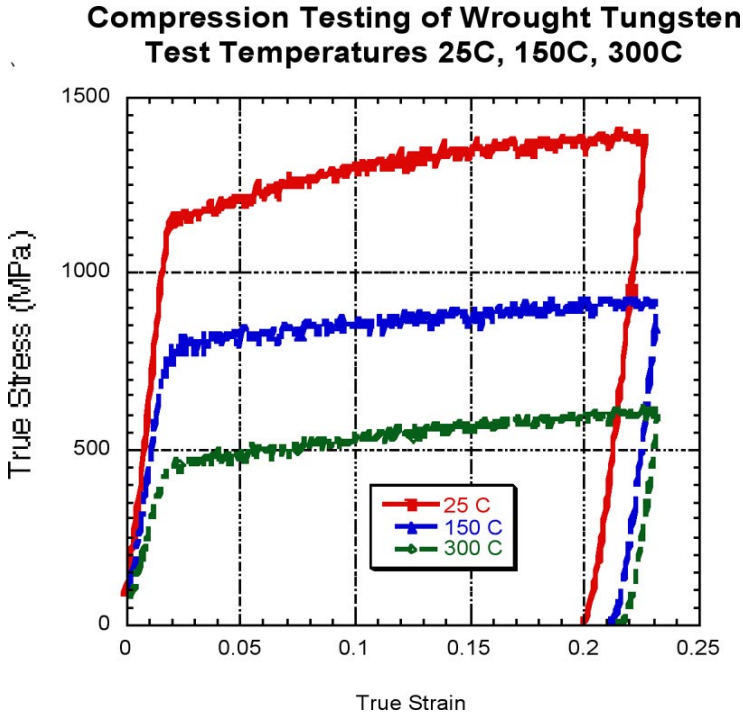

Fig. 2.6-1: Compression testing of wrought tungsten.

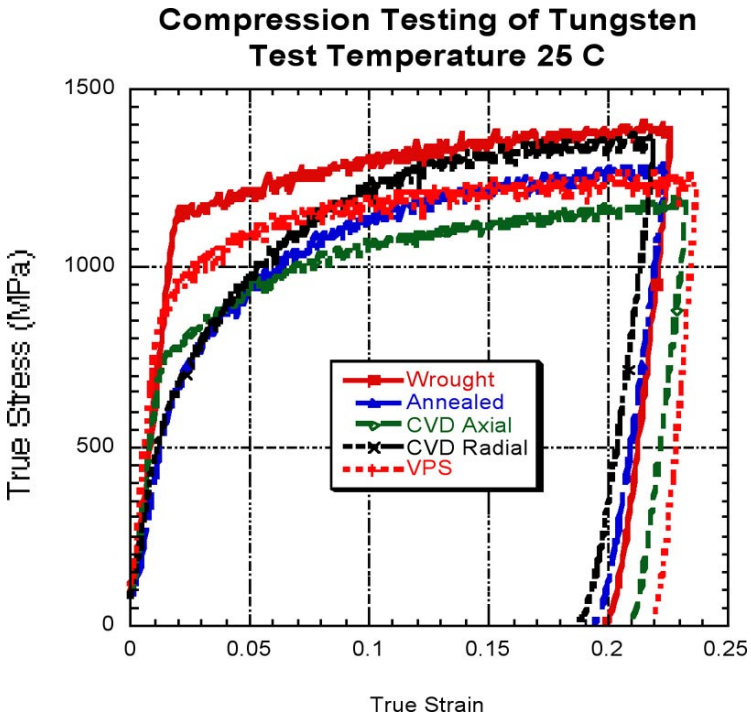

Fig. 2.6-2: Compression stress/strain curves tested at 25…C for tungsten.

Conclusions:
The yield strength is a function of the manufacturing process. For all the tungsten samples, the yield strength decreases substantially with increasing temperature.

For additional information, please contact Stuart Maloy (LANL) at maloy@lanl.gov .

2.7 AAA Materials Handbook

Objective:
The objective was to publish Rev. 3 of the materials handbook in FY02 including new chapters on 9Cr-1Mo and LBE.

Accomplishments:
The following revisions were made to the Materials Handbook as part of the Rev.3. all the new additions to the handbook was peer reviewed before incorporating into the handbook.

Chapter 19: 9Cr-1Mo (New Chapter)

Chapter 22: Lead-Bismuth Eutectic (New Chapter)

Chapter 7: Tungsten (Revised to update the effect of irradiation on yield strength and corrosion)

Chapter 2: Alloy 718 (Revised to update the corrosion section)

Chapter 3: SS-316L (Revised to update the corrosion section)

Chapter 4: Al-6061-T4 (Revised to update the corrosion section)

In addition a draft chapter for HT-9 was prepared and will be incorporated into Rev. 4 of the handbook.

Conclusions:
Materials handbook continues to be a valuable source for materials data used in designing ADSs. In FY03, the handbook will be extended to include additional materials for fast reactor applications.

For additional information, please contact Stuart Maloy (LANL) at maloy@lanl.gov .

3. LEAD-BISMUTH EUTECTIC RESEARCH

Objective:
The main objective of the lead-bismuth eutectic (LBE) research is to complete the construction and testing of the DELTA loop and start long-term testing. In addition, corrosion experiments and modeling, oxygen control strategy and oxygen sensor development. Development of other instrumentation for LBE applications are within the scope of the LBE research activities

Highlights:
The highlights for the FY02 Integration and Analytical Support activities are as follows:

- DELTA loop construction and operational testing is completed and the loop is ready for long-term corrosion testing.

- A series of corrosion experiments on various structural materials of interest were completed. In these experiments the oxide layers are mechanically, chemically and electro-chemically characterized under static and dynamic conditions.

- Corrosion model is improved to better predict the experimental data and a TRAC model is develop to simulate the DELTA loop operations under transient and steady-state conditions.

- A initial set of on-line corrosion probe conceptual options are developed (with one leading option) for potential implementation and testing in the DELTA loop.

- Considerable progress in made on oxygen control probe and calibration development. Two sensors were shipped to Sweden for use in their LBE loop.

Major Tasks:
Short summary reports are provided for the followings tasks completed in FY02:

3.1. DELTA Loop Operations

Objective:
The main objective in FY02 was to complete the construction and testing of the DELTA loop and to start long-term corrosion testing. To achieve this objective extensive testing of the loop, instrumentation and the data acquisition system must be performed. Testing of the safety related instruments and automatic shutdown logic is required to obtain approval for unmanned operations.

Accomplishments:
In the fourth quarter of FY02, the DELTA loop (shown in Fig. 3.1-1) was brought to a reliable operational status that allowed unattended operations.

The DELTA Data Acquisition and Control (DAC) system includes automatic controls for temperature and gas pressure distributions in the loop. It also handles all of the different shutdown conditions such as high temperature or high pressure. In case of a shutdown condition, the DAC program automatically opens drain valves and allows the liquid lead-bismuth to drain into the drain tank. All of the DAC functions were tested and tuned. Automatic cleaning gas control was also included into the main DAC program. All oxygen sensors were connected to the DAC system and the readings were consistent. The oxygen control system was operated successfully. The freeze plug in the venturi used for gas injection was melted and the liquid-metal level was maintained by balancing its pressure with the cleaning gas pressure.

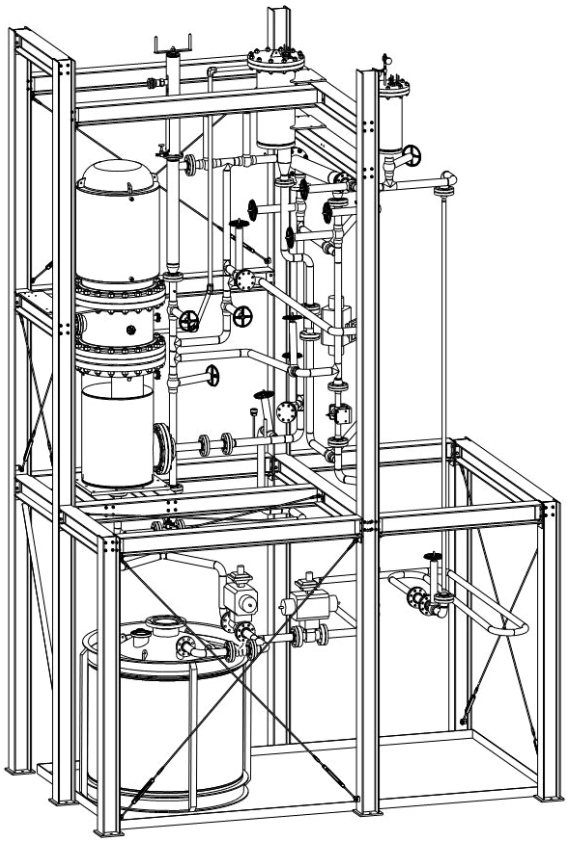

Fig. 3.1-1: Layout of the Delta Loop

DELTA loop was operated during the fourth quarter to test systems for unmanned operations. Total run time for testing the unmanned operations reached 120 hours. Overall, during the year the total run time was ~200 hrs. The first continuous 48-hour-long DELTA loop run was executed without problems. We ran at ~4.8m^3/hr flow rate and 60°C temperature gradient with minimum temperature of 345°C. The water-cooled heat exchanger was engaged during the entire run and performed consistently well. The Magnetic Flow Meter, however, did not function well during this run. The measurement was unstable and appeared to change with time. The decision was made to replace it with a more reliable venturi flow meter, and subsequent runs with the venturi flow meter proved successful. The readings were consistent with the theoretical predictions.

Pressure measurement in LBE proved difficult. Two kinds of pressure transducers failed after only several hours of operation. Investigation showed that solidifying liquid metal might damage the transducers diaphragms. The high temperature may also affect the electronics. We purchased more sophisticated and more robust pressure transducers made for higher temperature applications. We also devised a gas blow off system that sends a jet of gas at the transducers diaphragms blowing off the liquid metal and thus preventing it from solidifying on the diaphragm. The gas system was installed and linked to the DAC. We have already operated it and are working on tuning the valves dynamics to ensure the best results. In addition to repairing the liquid-metal pressure-measuring system, we had to repair or replace several other items on the loop:

- All oxygen sensors fittings welded to the loop piping had to be replaced. This was a preventative measure after a weld inside one of them failed.
- A new fitting for the gas injection inlet was designed and installed.
- The heat exchanger had to be disassembled to find cause of a water leak caused by a bad seal because of an error in manufacturing tolerance. The defect was fixed. No water leaks have been observed since the repair.
- We relocated and replaced several trace heaters and thermocouples for more uniform temperature distribution and control.
- National Instruments hardware used for DAC malfunctioned. New data acquisition modules were installed, thereby resolving the DAC hardware error.

Another major accomplsihment in preparing the loop for operations was the testing and calibarion of the oxygen sensors. The two oxygen sensors in flowing LBE read stable signals at the expected level, and responded correctly to LBE temperature fluctuations due to trace heater regulation (see Fig. 3.1-2). The sensors received several thermal shocks on the order of 10¡C during the loop fill.

Also a sample holder design shown in Fig. 3.1-3 was completed for the corrosion experiments. The corrosion test specimens, including 12 different materials and welds (T-91-316L) were fabricated and received for DELTA Loop tests. The specimens have been separated into corrosion test bar specimens and dog-bone type miniature tensile test specimens, and are awaiting final surface treatment.

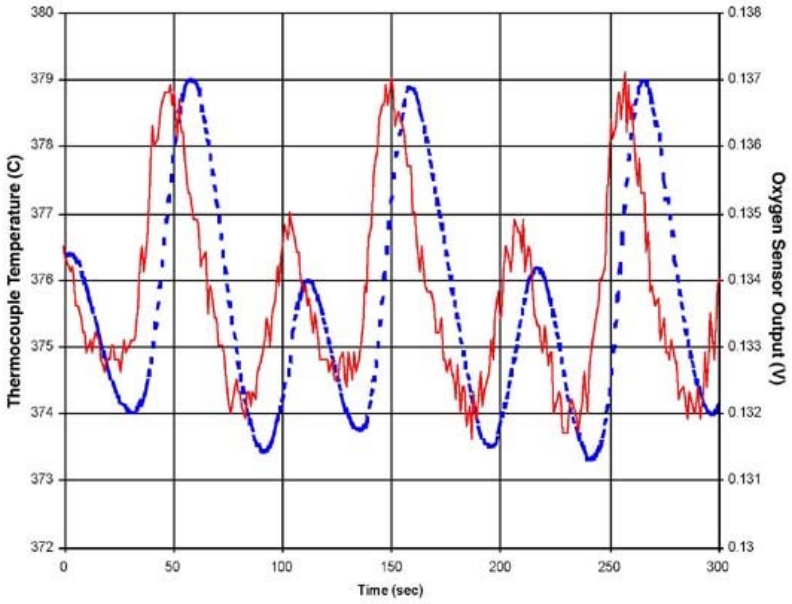

Fig. 3.1-2: Oxygen sensor readout during DELTA Loop operation.

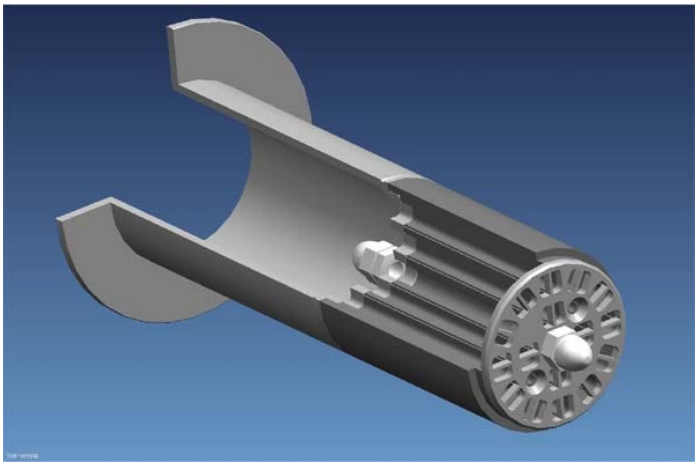

Fig. 3.1-3: DELTA Loop corrosion test sample holder design.

Finally, another noteworthy activity was the assessment of Ultrasonic Doppler Velocimetry (UDV). The report, Adaptation of Ultrasonic Doppler Velocimetry (UDV) to Measurement of LBE Flows, was issued, summarizing the working principles of UDV, the selection of US probe parameters, the coupling and transmission of US through container walls into fluids, and the reported experience in the literature. It will establish the needs, the requirements and a technical path forward for the LBE technology development. To adapt ultrasonic (US) transducers to the working temperature of LBE systems requires careful extension and coupling considerations. One of them is to minimize the transmission loss through interface steel structures for the high signal levels needed for UDV. Due the acoustic mismatch between steel and LBE, it is found that the thickness of the steel interface plate should be multiples of half the half-wavelength, or the loss could amount to more than 15%.

Conclusions:

As a result of the extensive work described above DELTA loop can be operated reliably unattended for long periods of time (hundreds of hours). The DELTA loop will be ready for the first materials test at the beginning of November. We are planning on 333-hour, 666-hour and 1000-hour tests with materials samples inside the test section.

For additional information contact Valentina Tcharnotskaia (LANL) at valentina@lanl.gov or Ning Li (LANL) ningli@lanl.gov .

3.2. Corrosion Experiments

Objective:
The objective was to investigate the corrosion phenomena for different alloys exposed to LBE by studying the fundamental mechanisms and oxide layer characterization.

Accomplishments:
Samples of HT-9, 440A, and SS-316L were oxidized in LBE at 400¡C for 330 hr and in air at 800¡C for exposures of 48 hr and 64 hr. Initial microscopy on HT-9 and 440A exposed to LBE found a thick (2 μm), compact, and adherent oxide film (Figs. 3.2-1). EDS maps of the LBE/oxide/metal regions found that

- the oxide consisted predominantly of Fe and Cr,
- the oxide was bi-layer: inner Cr-rich, outer Fe/Pb/Bi-rich, and
- the LBE immediately adjacent to the oxide film contained considerable amounts of alloy constituents Fe, Cr, and Mn

Preliminary capacitance measurements on samples oxidized in air and then exposed to LBE as a function of time and temperature have found several trends in both oxide capacitance and resistivity. In comparison, microscopy of SS-316L exposed to LBE found no oxide film at the delectability limits of the SEM (Fig. 3.2-1). It is uncertain whether this is because (1) a thin oxide film (tens of nm) is protecting the surface, (2) the surface oxide has not been wetted by the LBE, or (3) no oxide is present and there is an indication that an appreciable amount of corrosion has occurred. We are analyzing the thin LBE layer on the surface of the sample for corrosion product to establish whether or not an oxide film is present. Not surprisingly, given the lack of oxide scale, capacitance measurements on this sample were not successful. However, capacitance measurements on preoxidized SS-316 exposed to LBE as a function of time and temperature have found similar trends in both oxide capacitance and resistivity as observed in HT-9 and 440A steel.

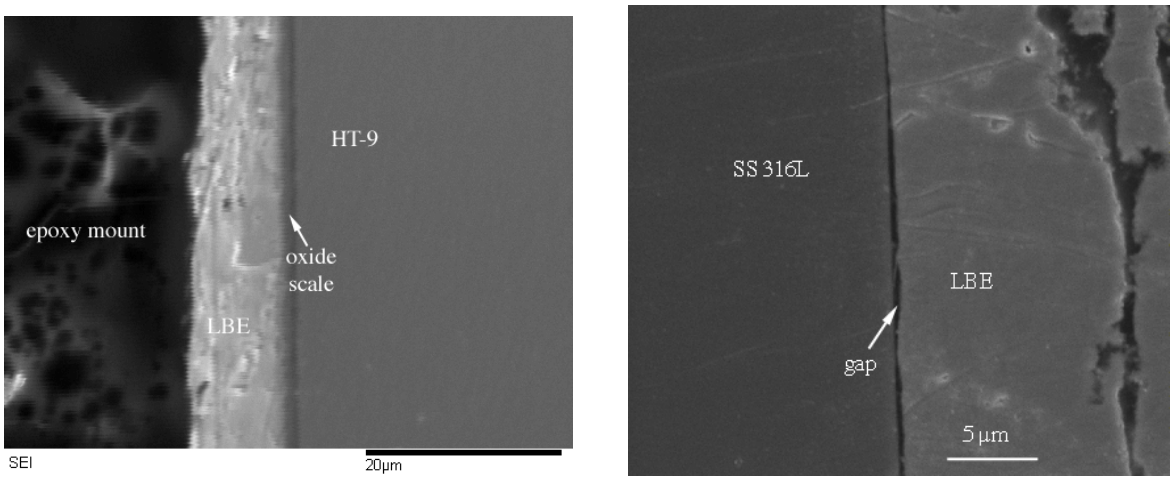

Fig. 3.2-1: Secondary electron image of HT-9 sample after exposure to LBE at 400¡C for 330 hr.

The dielectric and impedance properties of a variety of oxide films formed on HT-9 and SS-316L were characterized in liquid lead bismuth eutectic. Dielectric/impedance properties have been chosen as they reflect changes in transport characteristics that result in changes in corrosion rate. For example, substrates covered by an oxide with low specific capacitance and high impedance are generally resistant to oxidation. Thus, it may be possible to (1) use this technique to develop a real time corrosion probe for any LBE coolant system, (2) use this technique to optimize the pre-oxidation film formed in LBE loops, and (3) monitor the real-time influence of proton irradiation on oxide film properties.

Figure 3.2-2 shows the dielectric (capacitance) and impedance of oxide films formed on HT-9 in LBE as a function of pre-oxidation time (films formed in air at 800¡C). As can be seen in Fig 3.2-2, there appears to be an optimum pre-oxidation time of approximately 48 hrs. For this pre-oxidation time, the film impedance is maximized and the capacitance is minimized. Therefore, from these results one might conclude that the pre-oxidation conditions (prior to exposure to LBE) can be adjusted to minimize corrosion rate. Currently, these films are being investigated with TEM and surface analytical techniques such as XPS to establish the mechanism of "optimization."

The influence of LBE operating conditions on oxide properties also is investigated. For example, it is well known that oxide impedance decreases linearly with increasing temperature. An example is shown in Fig. 3.2-3. Here the impedance of an air-formed oxide film on HT-9 is measured by placing a gold foil on top of the film and measuring the impedance between the foil and the sample. On returning to room temperature, the impedance of the film returns to its original state. In addition, the increasing and decreasing impedance values are in fairly close agreement. However, when this identical experiment is run using LBE instead of the gold foil, a non-linear decrease in oxide impedance with increasing temperature was observed. In addition, a hysteresis between the increasing and decreasing temperature ramps was observed (Fig. 3.2-4).

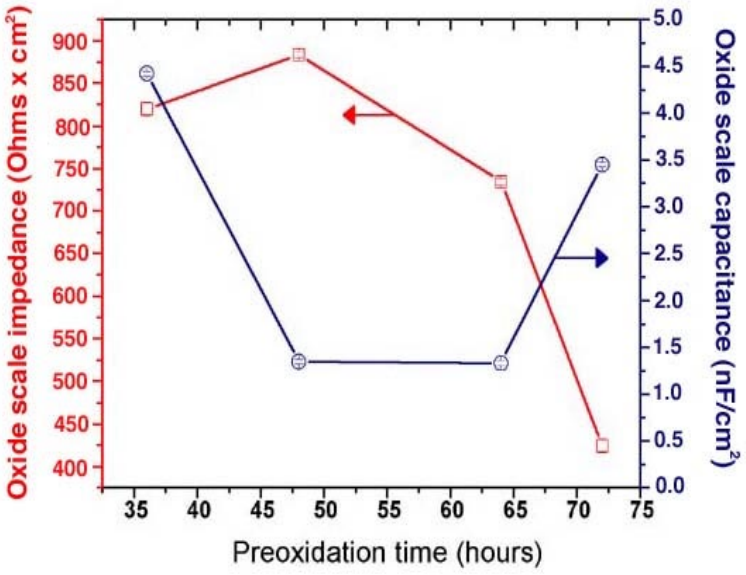

Fig. 3.2-2: Impedance and capacitance of oxides formed on HT-9 as a function of various oxidation times. All films were formed in moist air at 800°C.

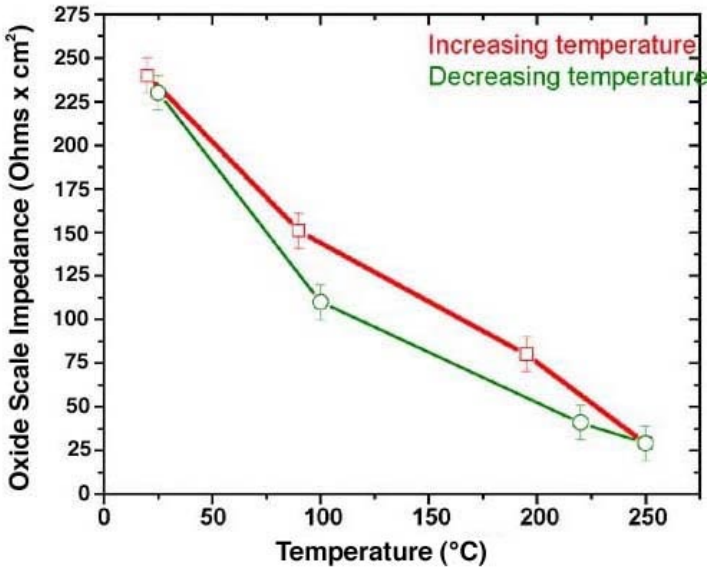

Fiig. 3.2-3: Impedance of oxide film on HT-9 as a function of temperature. Values were obtained by placing a gold foil on the oxidized sample and measuring the impedance between the sample and foil in air.

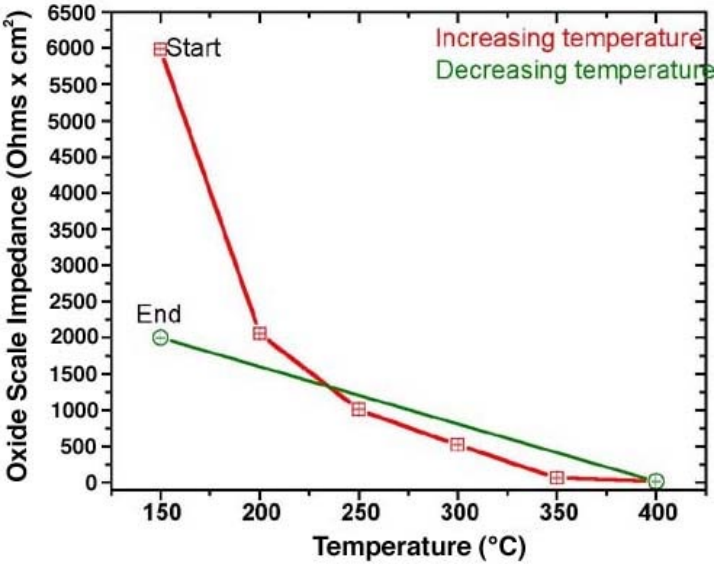

Fig. 3.2-4: Impedance of oxide film on HT-9 as a function of LBE temperature. Values were obtained by placing the oxidized sample in LBE and measuring the impedance between the oxide/LBE interface.

That is, the impedance of the oxide does not return to its original value at the end of the experiment; exposure to the LBE has changed the native properties of the oxide. Irreversible wetting of the sample is a simple and convenient explanation for this phenomenon. This is likely an incorrect model of the system, as the sample surface was in full contact with the LBE; and further, no change in the wetting angle for LBE on this oxide was observed (Figs. 3.2-5a and 3.2-5b) with increasing temperature. We propose that this phenomenon observed in LBE is a result of absorption of LBE into the outermost monolayers of the oxide. This could occur through diffusion, as one might anticipate a

temperature dependence on the diffusion coefficient as well as the kinetics associated with the transition from adsorption (wetting) to absorption. Understanding this mechanism is of importance because altering the step (by the addition of alloying materials, for example) could likely lead to materials with lower LBE corrosion rates.

Conclusions:
The fundamental understanding of the oxide layers and the protection against LBE corrosion is essential in developing a corrosion control strategy for using LBE in ADS or fast reactor applications

For additional information contact Scott Lillard (LANL) at lillard@lanl.gov .

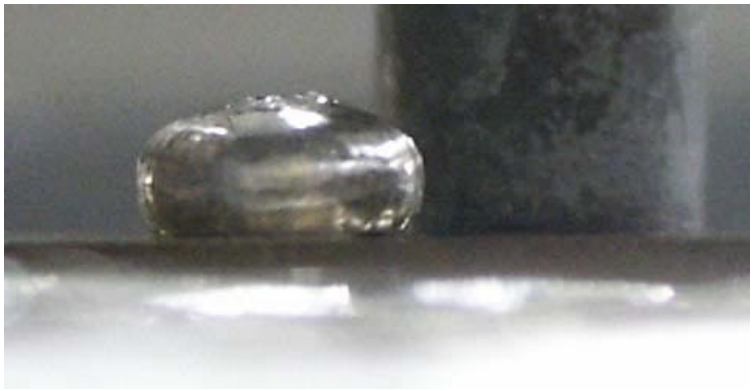

Fig. 3.2-5a: Wetting angle (~160¡) for LBE droplet on oxidized HT-9 at 210¡C.

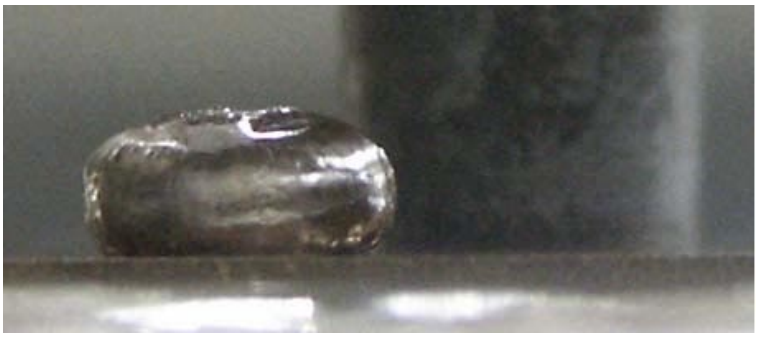

Fig. 3.2-5b: Wetting angle for LBE droplet on HT-9 at 300¡C.
(Wetting angle is the same as in Fig.˚3.2-5a at 210¡C, ~160¡)

3.3. Corrosion and Thermal-Hydraulic Modeling

Objective:
The objective was to update the previously developed corrosion analysis model and to set-up an analytic loop model to analyze the DELTA loop data as they become available.

Accomplishments:
Significant progress has been made on the modeling of corrosion in oxygen-controlled LBE systems. We have expanded the model to include multi-branch, multi-section variable cross-section loop systems, time evolution toward steady state, simple corrosion product reactions in the fluid, and other effects. This work has significantly improved the capability to predict the corrosion rates in oxygen-controlled LBE systems, and the ability to interpret and extend the use of corrosion test results. The system model, with analytical solutions in many instances, and numerical solutions for the more general cases, is used to parametrically study the corrosion and precipitation distributions in LBE systems, and to improve the system designs to accelerate corrosion in test systems and minimize corrosion in engineering applications. The improved model predicts corrosion rates in better agreement with the experimental results when loop dimensions are available.

Using this model, the average corrosion rate in the DELTA Loop test section is mapped against the test temperature and loop temperature difference (see Fig. 3.3-1). It is found that the corrosion rate increases drastically above 550¡C, and it starts to saturate after the temperature difference reaches 100¡C in the 500¡C— 550¡C range. This result proves that the selection of the DELTA Loop test condition is near optimal.

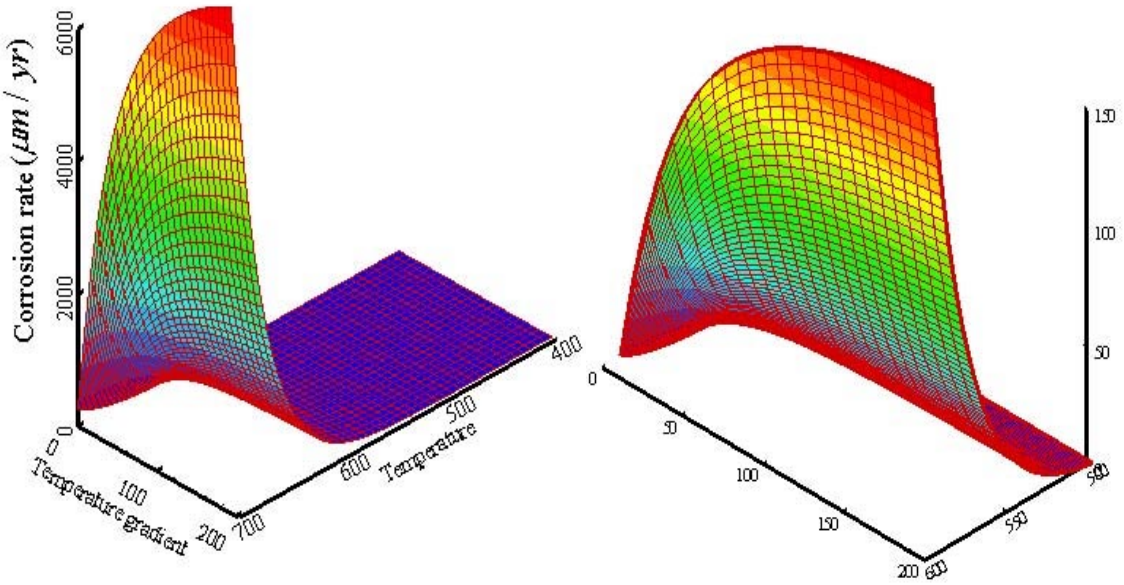

Fig. 3.3-1: Average corrosion rate in DELTA Loop test section for v = 0.6m/s, oxygen concentration of 10^{-6} wt%.

Also, a TRAC-code model for the DELTA Loop was developed with proper pipe sizes, elevation, and calculated loss coefficients (see Fig. 3.3-2). The model has been checked and calculated to steady state at several different mass flows and power settings. It will be benchmarked against the DELTA Loop test operation data.

Conclusions:

The analytic models to predict the corrosion in LBE are being improved. The TRAC model will be used for predicting the DELTA loop conditions and subsequently a similar model will be applied for MEGAPIE test.

For additional information contact Ning Li (LANL) at ningli@lanl.gov .

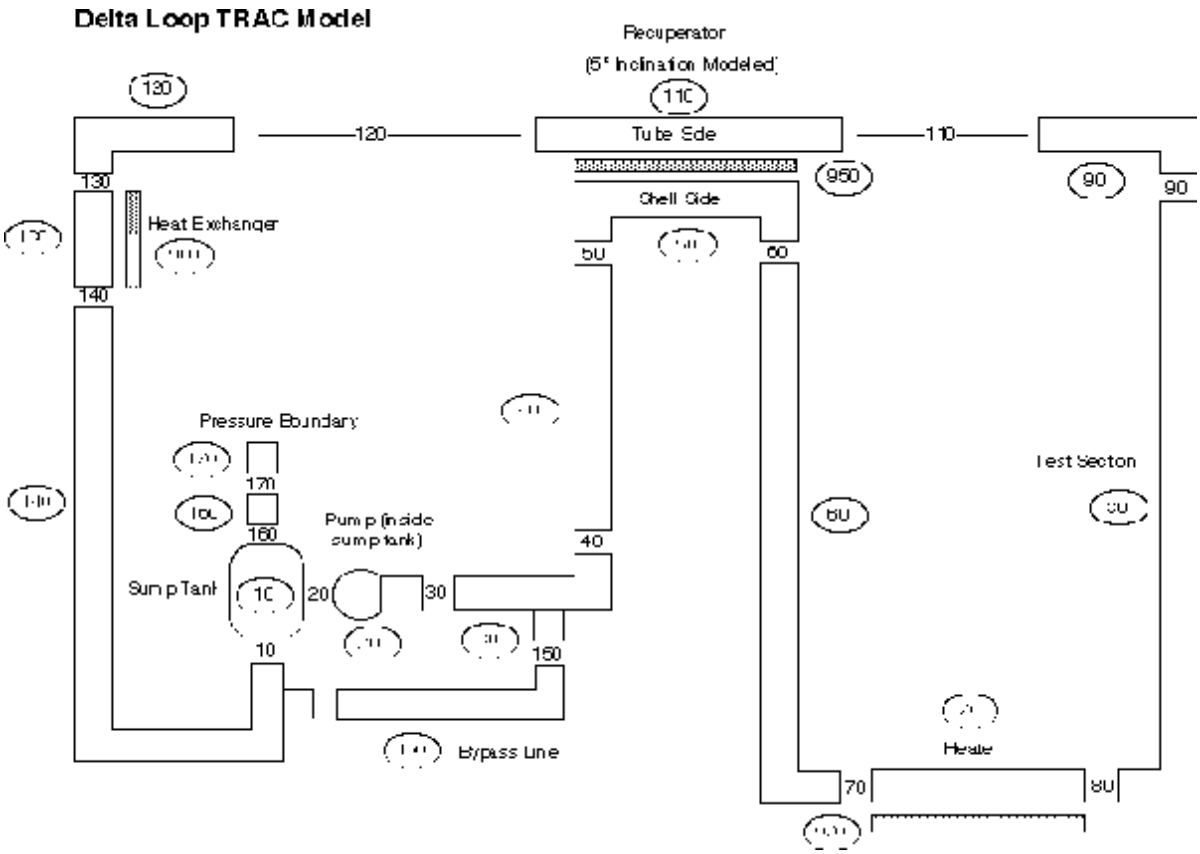

Fig. 3.3-2: DELTA Loop TRAC model.

3.4. Corrosion Probe Conceptual Design

Objective:
The objective was to develop the conceptual design of a corrosion probe based on oxide layer dielectric measurements. The probe will be built later and tested in the DELTA loop.

Accomplishments:
Analogous with the science of aqueous corrosion and its real-time measuring techniques, a corrosion probe for a molten lead-bismuth eutectic (LBE) system would measure in real-time the dielectric properties of the protective oxides. From these data one can obtain information such as oxide thickness, which is proportional to corrosion rate. Laboratory studies on candidate materials are in progress to determine the relation between the dielectric properties of the protective oxide layers (which are typically semiconductors) and the metallographic characterization of those oxides in other words, to understand the kinetics of metal corrosion in LBE. It is anticipated that the DELTA Loop will figure prominently in the determination of the relation between the properties of the oxide layers and measurable metal corrosion because long exposures are under controlled oxygen, flow, and temperature. Furthermore, the DELTA Loop could become an ideal laboratory for the kinetics studies provided that corrosion probes can be successfully introduced.

In laboratory studies, metals samples are partially immersed in LBE with air or a gas covering the LBE. An LBE corrosion probe suitable for use in the DELTA Loop must have the following characteristics:

- It must be electrically isolated from the loop piping in order to measure the dielectric properties of the oxide surface.
- The insulator and the metal-to-insulator joint must withstand the pressure, fluid forces, temperature, and the corrosive effects of the LBE.

Although several designs have been proposed in our end-of-year report, here, we believe the tapered design shown in Fig. 3.4-1 will be the most successful from an operational standpoint (although it may be somewhat complicated to manufacture). The aspect ratio of the insulator is adjusted to accept very high axial loads during the pressing of the upper and lower joints. A most important improvement calls for a ceramic with a larger coefficient of thermal expansion, and there is frequent mention of zirconia in the range of $10.5 \times 10^{-6}/^{o}C$, which is excellent for use with HT-9 and adequate for T-91. With a press fit on such a ceramic, differential expansion uses up only 20% of the elastic strain of HT-9 and, less favorably, 38% of the elastic strain of T-91.

A second design condition is that stress relaxation (related to creep) not loosen the joint. For T-91, the creep rate is 1×10^{-7} per hour at 270 Mpa and 755K. For 1000 hours at temperature, the creep strain is 7% of the elastic strain, which is quite acceptable. It might be assumed that only 7% of the elastic stress will relax at zero strain under the same conditions (note also that the stress quoted is 70% of the yield stress in order to obtain the low creep rate). The high temperatures materials are thus able to maintain high compression on the seal and the sealing surfaces during temperature cycles. The optimum condition for the metals is possibly the annealed state prior to the final press. Work hardening is minimized in this way, which helps also with minimizing stress relaxation.

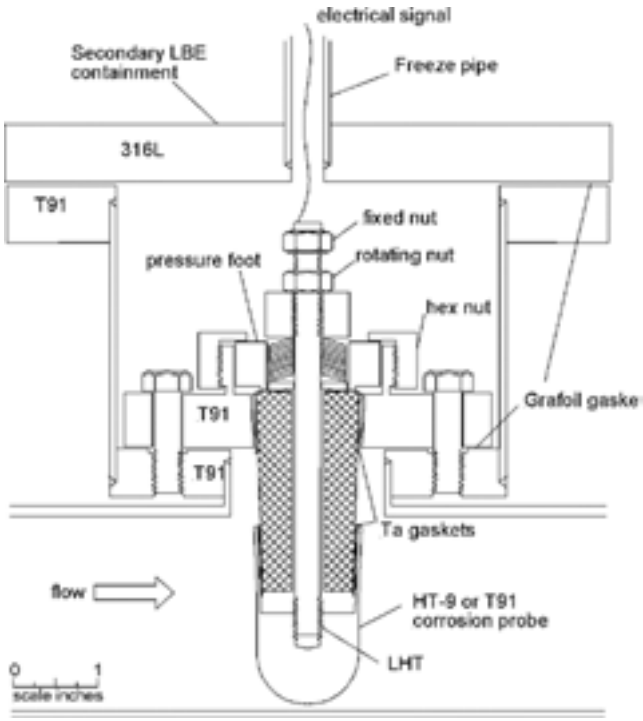

Fig. 3.4-1: Cross section through a Ta-sealed press-fit assembly with a 3° taper for upper and lower joints.

The retainer nut is not expected to drive the cone into the flange; its purpose is to align the pressing foot, to start the joint with good alignment[2] and to help maintain alignment as pressing proceeds. The corrosion probe seal is pressed next and is likewise not constrained. Hence, the probe wall thickness should be the maximum that still permits the probe to press onto the insulator without breaking it. In this way large pressures can be generated in the tantalum (at 200°C) to extrude it into the cracks and scratches and to form a crevice-free seal at the top edge. Fixturing is possible where the center bolt can be tightened as pressing proceeds. Here again, the bolt is intended to start the pressing with good alignment and to maintain the alignment. And then, particularly for T-91 probes, it ensures that the joint stays tight during thermal cycles.

Conclusions:
The proposed conceptual design has a high likelihood for successful implementation in the DELTA loop. The design is the most robust of the free standing probes; the joint has the potential to form a helium-leak seal; if necessary, it could work without tantalum (and has); and may even simplify to a version without threaded retainers. The biggest detractor is inability to accommodate SS-316L.

For additional information contact Scott Lillard (LANL) at lillard@lanl.gov .

[2] The pressure face must be exactly parallel to the thread for there to be any alignment benefit.

3.5. Oxygen Control Technology

Objective:
The objective is to develop oxygen control technology for LBE technology applications in transmutation. Development, construction and calibration of reliable oxygen sensors are within the scope of this work. Strong International collaboration is essential in achieving the objective within the time period supporting the AFCI decision deadlines.

Accomplishments:
In FY02, we designed the hydrogen and steam gas-mixture system for gas-phase oxygen control and calibration of oxygen sensors. It consists of a gas flow-control manifold, a steam generator, a gas-mixing chamber, and RGAs for measuring compositions. The device is shown in Fig. 3.5-1. Two RGAs were calibrated to measure hydrogen, helium, and oxygen to levels of a few parts per billion in mass concentration. Gas supply and system purity was tested. It was concluded that the residual oxygen levels in helium, although too high if directly used in LBE, should not affect the gas-mixture system s control of the oxygen level in LBE. The oxygen-sensor calibration system has achieved the stringent system tightness requirement needed for the calibrations. A series of calibration curves are shown in Fig. 3.5-2 for two sensors.

The LBE in the rocking U-tube calibration apparatus was cleaned by a 6% H_2/He mixture at a temperature between 440¡C—500¡C to a desired oxygen level as indicated by the OS, after which the gas supply was terminated and the system shut off. After some time, the temperature of the LBE gradually decreased while the OS output is continuously reported the corresponding temperature. The OS voltage-vs-temperature curves obtained so far are for constant oxygen concentrations. After initial transients, the curves display the linear trend with slopes very close to theoretical values as illustrated in Fig. 3.5-2. As was confirmed in the experiment, when the LBE temperature reaches the point where the oxygen becomes saturated, the voltage no longer follows the constant-concentration curve but instead tracks the saturation-limit curve.

There are two experimental difficulties: (1) Because there is residual hydrogen left in the cover gas after the system is closed, the oxygen concentration is slightly reduced and is perhaps the reason behind the flatter calibration curves near the start of the runs; and (2) When oxygen reaches the saturation limit as temperature decreases, the excess oxygen comes out in the form of lead oxide a phase transition process involving nucleation, mass transport and precipitation and is difficult to measure. Overall, it is very difficult to maintain the system tightness for more than two days. A report on oxygen control methodology and sensor calibration strategy was issued, detailing the advantages and disadvantages of gas-phase and solid-phase oxygen control, and providing key implementation guidelines. The oxygen sensor calibration standard is established, and several alternatives for cross calibration and validation are outlined.

Preparation of the oxygen sensors, especially with the addition of sufficient bismuth oxide and the cleaning of the ceramic surface, was improved during the experiments for more consistent sensor response and the ability to measure the extremely low oxygen concentration at the magnetite dissociation limit (oxygen concentration in that range is below ppb and approaching 10^{-12}).

Fig. 3.5-1: An oxygen control and sensor calibration system.

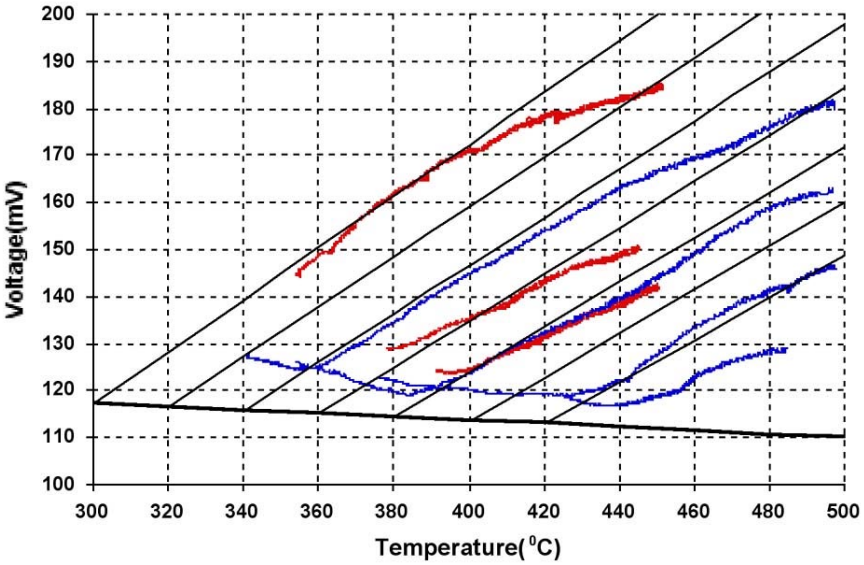

Fig. 3.5-2: Oxygen sensor calibration curves for two sensors (red and blue). The solid lines are theoretical values for constant oxygen concentrations (not computed for the OS data), and the bold solid line is at the oxygen saturation limit in LBE.

From Fig. 3.5-3, we find that the oxygen sensor has very low output voltage (close to zero) before the reference electrode Bi (saturated with oxygen) is melted. Once the Bi is molten, the output voltage increases to a level corresponding to oxygen saturation in LBE as expected since the LBE in the DELTA Loop has not been cleaned with hydrogen. As the temperature rises, the dependence of the output voltage of the oxygen sensor on temperature follows a linear trend. This trend can be calculated from the thermodynamic data and the oxygen solubility in LBE. The experimental results agree well with the theoretical prediction, indicating that the LANL-developed YSZ | B/Bi_2O_3 sensors may follow the Nernst equation down to the melting point of Bi. Even if it deviates from this ideal relationship, this type of sensor may be calibrated to give proper reading of the oxygen activity in LBE down to 270°C if the reliability and consistency can be proved.

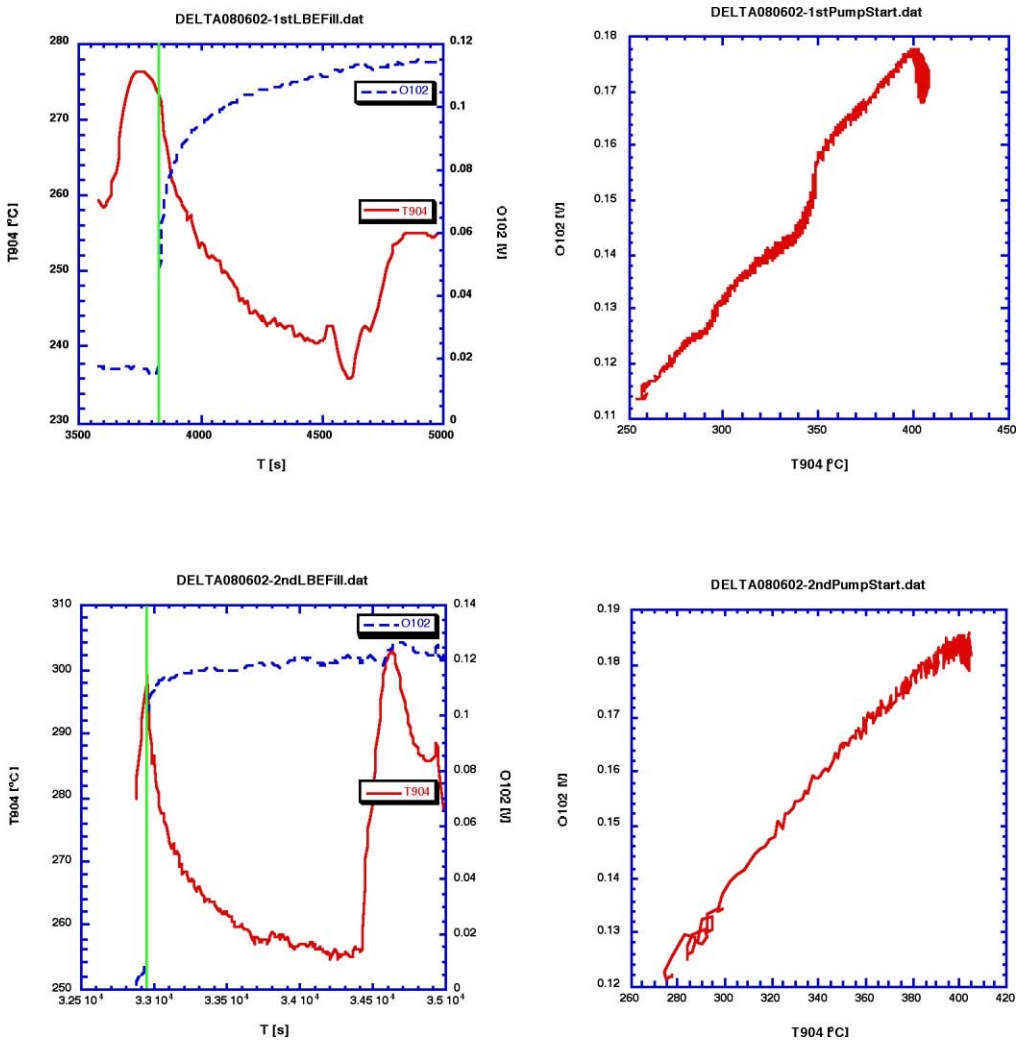

Fig. 3.5-3: YSZ | B/Bi_2O_3 oxygen sensor response to temperature changes in DELTA Loop (08/06/2002 operation data).

Low Temperature Oxygen Sensors for LBE Systems [3] was completed and issued, summarizing needs, requirements, and existing literature results on low temperature oxygen sensors, examining the preliminary experimental results of YSZ-based sensors in that temperature range, and presenting a path forward for future development. In several experiments performed in the DELTA Loop and the oxygen sensor calibration apparatus, the behavior of such sensors at temperatures below 350¡C can be determined, although a more systematic study will be needed to quantitatively characterize sensor response.

Two LANL-made oxygen sensors were approved for export and delivered to a research group in the Royal Institute of Technology (KTH), Sweden (see Fig. 3.4-4). The sensors will be installed into a LBE natural convection loop studying reactor core cooling. Sensor specifications were also sent to the MEGAPIE project.

[3] LANL Report, LA-UR-02-6428

Fig. 3.4-4: Two LANL-developed YSZ|B/Bi_2O_3 oxygen sensors delivered to KTH, Sweden.

Conclusions:

The next phase of the investigation will focus on more systematic calibration runs, improvement of sensor design and assembly, tabulation of calibration curves with uncertainty and variability bounds, and increasing the partial pressure of hydrogen- and-water steam mixture for measuring the partial pressure of oxygen. The data will be provided to the International LBE handbook effort initiated under the OECD/WPPT. Close collaborations with International partners will continue in oxygen control technology.

For additional information contact Ning Li (LANL) at ningli@lanl.gov .

4. LANSCE IRRADIATION EXPERIMENTS

Objective:
The main objective was to obtain fundamental proton and neutron irradiation data for technologies relevant to transmutation using the Weapons Research Facility (WNR) and the Blue Room in LANSCE.

Highlights:
The highlights for the FY02 LANSCE Irradiation experiments are as follows:

- A final report of the sodium-activation tests is issued in FY02 summarizing the results of sodium activation tests performed in FY01 (LA-13902-MS).

- A preliminary status report summarizing the results of the 20-cm LBE target experiments was published (LA-UR-02-5552). Also, the measurements with a 40-cm target were completed and the data are being analyzed.

- Helium and hydrogen production data on iron samples were collected and the data are being analyzed.

- A series of impedance measurements on oxide films subjected to proton beam irradiation were made during irradiation. The data are being analyzed for a final report.

Major Tasks:
Short summary reports are provided for the followings tasks that were completed in FY02:

4.1. Sodium Activation Tests

Objective:
The irradiation of sodium cans using 800 MeV beam was completed in FY01. The sodium can is shown in Fig. 4.1-1. Because of budget constraints, irradiations at different beam energies were postponed. The objective in FY02 was to complete the data analysis and to publish the results.

Accomplishments:
The measured activities were corrected for the decay after irradiation and branching rations, and then converted to cross-sections using the measured proton fluence and sample thickness. Data for the cross-sections derived from the four different counts were used to form a weighted average using the statistical uncertainties associated with each separate measurement. The statistical uncertainty on the average value was then combined with the various systematic uncertainties to produce the final overall uncertainty. The derived cross-sections are listed in Table 4.1-1.

MCNPX (version 2.1.5) was used to model the experimental geometry. The calculated yields of isotopes were then used to determine production cross-sections. Additional MCNPX calculations were then performed to estimate production cross-sections for proton energies 100–800 MeV using the standard high-energy physics model in MCNPX (Bertini without a pre-equilibrium phase). Further calculations were performed using the ISABEL (physics modeling code) and CEM (Cascade Exciton Model code) high-energy physics models available in MCNPX. Results are shown in Table 4.1-2. Results indicate that the Bertini model most closely calculates the ^{7}Be production cross-section, although the C/E is only 0.65. The ISABEL physics model is slightly better than the Bertini model for the ^{22}Na production cross-section (C/E=1.47). However, improvement in the estimate is only ~5% over the Bertini model.

Fig. 4.1-1: The sodium can used in the irradiation

Table 4.1-1: Measured Cross Sections and Uncertainties

Isotope	Cross Section (mb)	Uncertainty (mb)
^{7}Be	6.50	0.24
^{22}Na	29.45	1.00

Table 4.1-2: MCNPX Calculations of ^{7}Be and ^{22}Na Production Rates in Sodium Sample

High-Energy Physics Model	Proton Energy (MeV)	Be-7 Production				Na-22 Production			
		(atoms/ proton)	error	X-section (barns)	error (barns)	(atoms/ proton)	error	X-section (barns)	error (barns)
Bertini	100	3.05E-07	0.378	2.40E-05	9.09E-06	8.52E-04	0.0072	6.71E-02	4.83E-04
Bertini	200	2.87E-06	0.1078	2.26E-04	2.43E-05	6.98E-04	0.0069	5.50E-02	3.80E-04
Bertini	300	6.43E-06	0.072	5.07E-04	3.65E-05	6.44E-04	0.0072	5.07E-02	3.65E-04
Bertini	400	1.38E-05	0.0491	1.09E-03	5.35E-05	6.32E-04	0.0073	4.97E-02	3.63E-04
Bertini	500	2.27E-05	0,0383	1.79E-03	6.86E-05	6.21E-04	0.0073	4.89E-02	3.57E-04
Bertini	600	3.67E-05	0.0302	2.89E-03	8.72E-05	6.14E-04	0.0074	4.83E-02	3.58E-04
Bertini	700	4.51E-05	0.0272	3.55E-03	9.67E-05	5.96E-04	0.0075	4.70E-02	3.52E-04
Bertini	800	5.39E-05	0.0249	4.24E-03	1.06E-04	5.77E-04	0.0076	4.54E-02	3.45E-04
Isabel	800	2.61 E-05	0.0357	2.06E-03	7.34E-05	5.50E-04	0.0076	4.33E-02	3.29E-04
CEM	800	9.33E-07	0.189	7.35E-05	1.39E-05	6.35E-04	0.0073	5.00E-02	3.65E-04
Bertini/ pre-equilibrium	800	5.39E-05	0.0249	4.24E-03	1.06E-04	5.77E-04	0.0076	4.54E-02	3.45E-04
Data	800			6.50E-03	2.40E-04			2.95E-02	1.00E-03

Conclusions:

The data shows that the models underpredict the Berilium-7 production and overpredict the Na-22 production. If a sodium-cooled target option is used for transmuter applications, additional data at different energies would be necessary to improve the code predictions.

For additional information contact George Morgan (LANL) at gmorgan@lanl.gov or Ray Klann (ANL) at klann@anl.gov .

4.2. LBE Target Neutron Yield and Spectrum Tests

Objective:
The goals of the initial target irradiation experiment were to: (1) provide initial experimental data for planning future irradiation campaigns, (2) provide experimental data of benchmark quality that can be used for validation of MCNPX, (3) provide experimental quantification of high-energy particle leakage out of an LBE target, with varying size for structural damage data analyses, and (4) further develop methods and improve techniques for spectral unfolding using integral reaction data from activation foils.

Accomplishments:
The first series of experiments consisted of irradiating a solid LBE target (dia=20 cm, L=50 cm) with an 800-MeV proton beam of 20-25 nA and measuring the neutron emission from the target by two methods — activation foils and time-of-flight (TOF) measurements. The foil packets consisted of several foil materials packaged together for simultaneous irradiation. The materials used for most foil packets were Bi, Nb, In, Co, Ni, Cu, Fe, Al, Au, Cd-covered Au, Rh, Ti, Zn, Lu and Tb.

After an initial irradiation, the foils were removed from the target and counted via gamma spectroscopy. Irradiation of the target continued with TOF measurements performed at 7.5¡ and 30¡ beam-tubes. Also, two foil packets of identical composition to the Blue Room packets were irradiated in a known neutron spectrum to test the spectral unfolding process. The results from those packets show a good fit to the spectrum.

Two gamma detectors were configured at LANSCE to count the foils. Additionally, many foils were sent to the other locations at LANL and analyzed there. Initial results from the Bi foils irradiated in the Blue Room show a definite change in the hardness of the neutron spectrum over the length of the target with the spectrum decreasing in intensity but increasing in average energy as one gets further from the front face. These results are as expected, based on target modeling in MCNPX.

Results of the first irradiation indicate that both techniques for measuring the neutron leakage provide useful and complementary information. The activation foils provide significant quantities of integral reaction data that can be used for spectral unfolding with errors representative of the uncertainties in the nuclear data. The TOF measurements provide very detailed information regarding the neutron spectra in a small solid angle (i.e. double differential data). The neutron energy spectra obtained from the TOF data are shown in Fig. 4.2-1.

The second phase of the Blue Room Neutron Yield Experiment was performed in July. A 40-cm diameter LBE target was irradiated. For the 40-cm target, TOF data were taken from 4 beamlines around the target, at 7.5°, 30°, 60°, and 150° from the target (and proton beam) axis. Activation foils were placed at intervals along the axial length of the target and at 45° radial intervals at the z=15 and z=40 cm axial locations. The target positioned in the Blue Room is shown in Fig. 3.2-2.

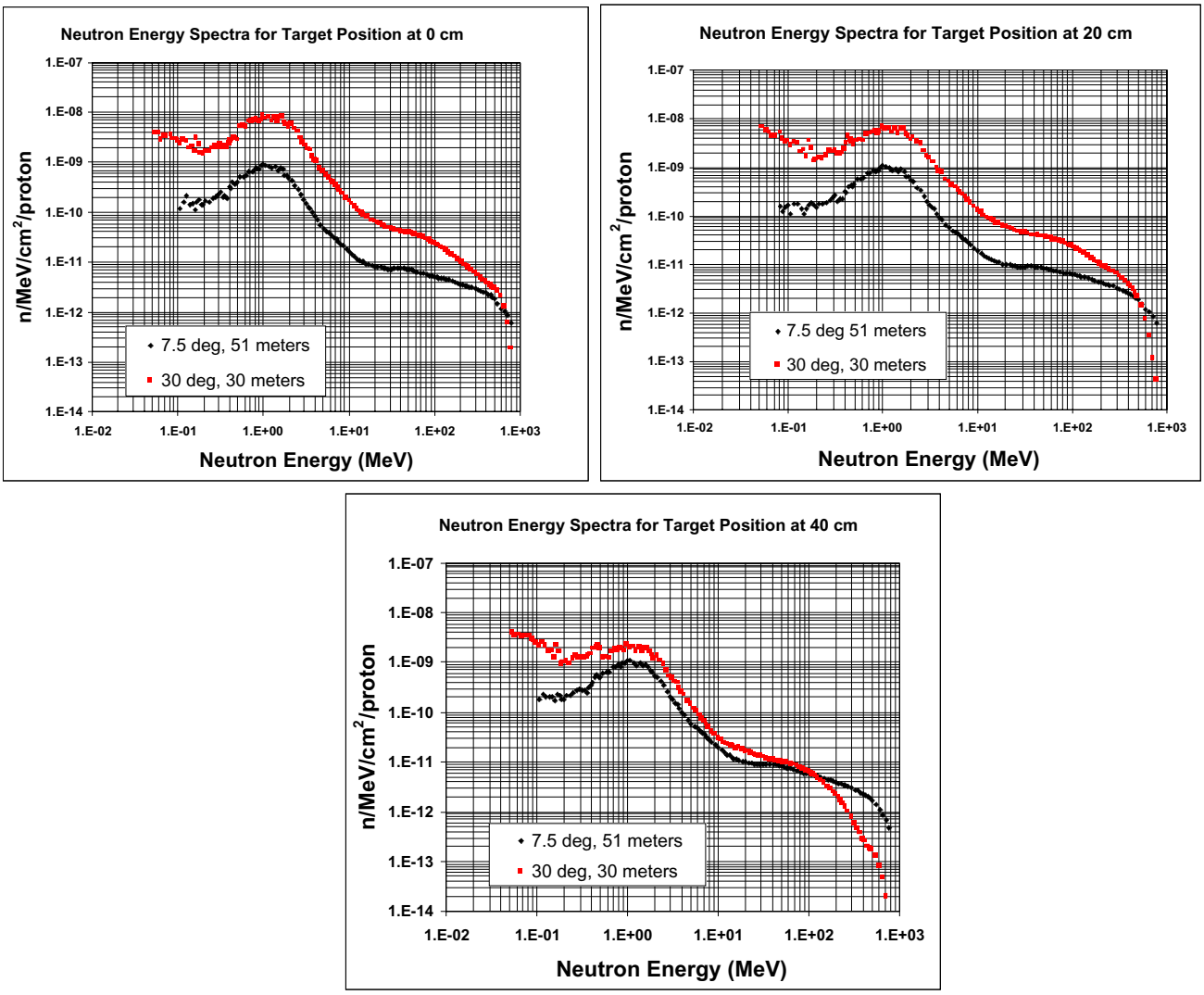

Fig. 4.2-1: Neutron-energy spectra for target position at 0. 20 and 40 cm.

Fig. 4.2-2: 40-cm diameter target in the Blue Room.

After this sequence of irradiations, the 40-cm target was removed and the 20-cm target placed in position. No activation foil analyses were performed, but TOF measurements were made for the purpose of gathering data at the 60° and 150° angles that had not been used with the previous irradiation of this target.

Initial analysis of the results from the 40-cm target irradiation has focused on the Bi foils. An analysis of three different gamma energies from the decay of ^{204}Bi is given in Figs. 4.2-3 and 4.2-4. These results show a slight asymmetry, most likely from small misalignment of the proton beam with the target axis. The shape of the neutron flux has also been analyzed from the Bi data. Further analysis of the activation foils data will be undertaken to examine the neutron spectra at various locations in detail.

Conclusions:

The irradiation experiments for the targets with 20- and 40-cm diameters were successfully completed. Initial analyses show that the tests provided valuable data for benchmarking and accurately quantifying the high-energy particle leakage from the target. Unfortunately, the last set of experiments with a 10-cm target was cancelled due to funding constraints. This smallest target would have provided the maximum high-energy particle leakage data. These experiments were also quite useful to support university participation and graduate student education. UNLV is providing computational support with MCNPX modeling of the neutronics and CAD modeling of the experimental configurations. UM is providing assistance in neutron data and spectrum unfolding as well as long-term counting of foils. Both schools contributed summer students who arrived at LANL in mid-June for six-week appointments.

For additional information contact George Morgan (LANL) at gmorgan@lanl.gov , or MikeJames (LANL) at mrjames@lanl.gov , or Ray Klann (ANL) at klann@anl.gov .

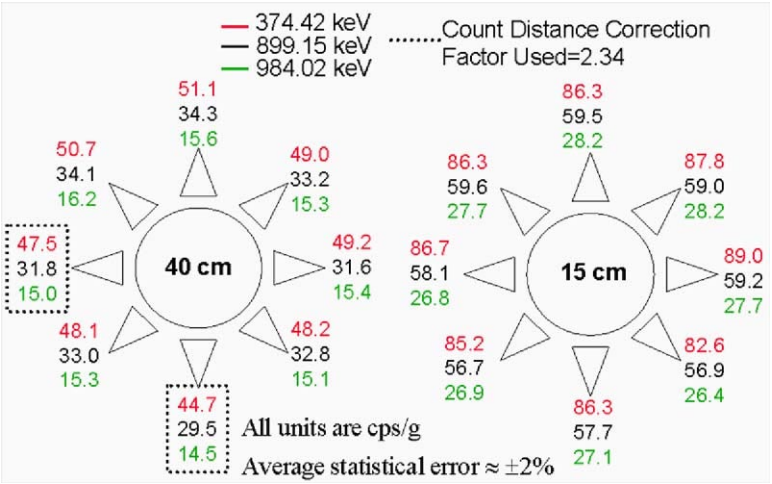

Fig. 4.2-3: Radial asymmetry ion the Bi-204 decay.

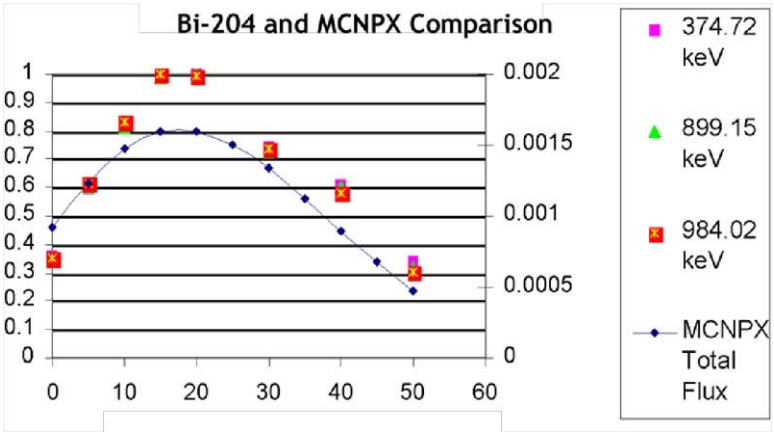

Fig. 4.2-4: Neutron intensity as a function of axial position from Bi-204 results.

4.3. Helium and Hydrogen Production Tests

Objective:
Hydrogen and helium are produced when energetic neutrons interact with materials, and these gases can lead to significant changes in material properties such as embrittlement and swelling. We are measuring gas production cross-sections for materials of interest from 1–100˚MeV covering the range applicable to fast reactors and ADS.

Accomplishments
In the first quarter of FY02, we commissioned the detector station to measure hydrogen and helium production cross-sections as functions of incident neutron energy. In this experiment, we used a thin foil of the material so charged particles can escape and be detected. We measure charged particles with detector systems at many angles. The test chamber is an evacuated chamber, 55.9 cm I.D., to accommodate the test materials and the detectors. The apparatus is located on the 30-degree right beam line at the LANSCE/WNR spallation neutron source. Detectors are coincidence counters consisting of low-pressure gas-proportional counters followed by silicon surface-barrier detectors and thick CsI(Tl) detectors to stop the most energetic hydrogen and helium nuclei. Signals from these detectors undergo preliminary processing near the chamber, and then the processed signals are transported to further electronics and a data acquisition system in a nearby building. The chamber and the detector layout are shown in Fig. 4.3-1. Each detector system consists of two or three detectors in coincidence and arranged so the charged particles pass through the first detector and stop in the second or third. We do this to identify the protons, deuterons, and alpha particles and also the small numbers of tritons and ^{3}He. The commissioning experiments included a test run on an iron sample. Data from our first run are shown in Fig. 4.3-2 to illustrate the good identification of the charged particles and, qualitatively, the good counting rate.

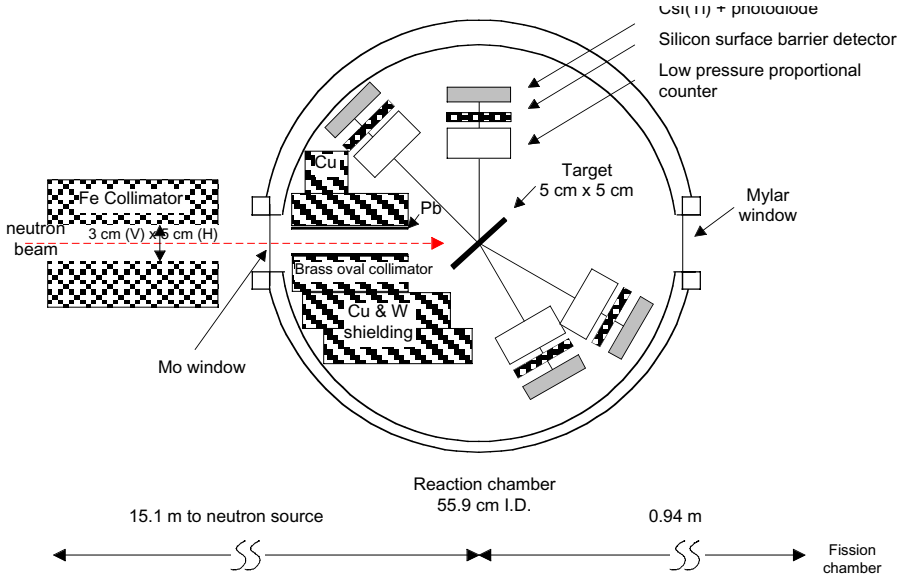

Fig. 4.3-1: Layout of the test apparatus.

Subsequently, we analyzed the data from the commissioning tests and we improved the experimental setup in preparation for beam in the fourth quarter. The improvements included (1) improving the collimation and shielding in order to reduce backgrounds; (2) improving the light collection efficiency for the scintillator. Early results for the production of protons with energies above 14 MeV on iron (collected in the fourth quarter) are shown in Fig. 3.4-3 as a function of incident neutron energy. Lower energy protons were also detected and we will be able to give total proton production when the data analysis is completed. The forward-angle production is clearly dominant.

Conclusions:
The experiments on irons samples worked very well. The data analyses for iron will be completed in FY03. In addition, data for chromium and nickel will be collected in FY03.

For additional information contact Bob Haight (LANL) at haight_robert_c@lanl.gov .

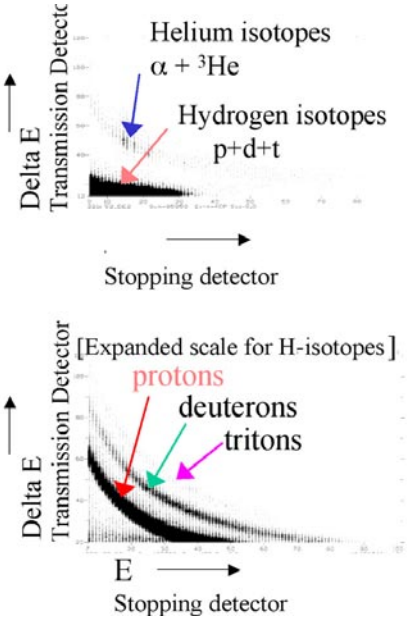

Fig. 4.3-2: Identification of protons, deuterons, tritons, ^{3}He, and alpha particles.

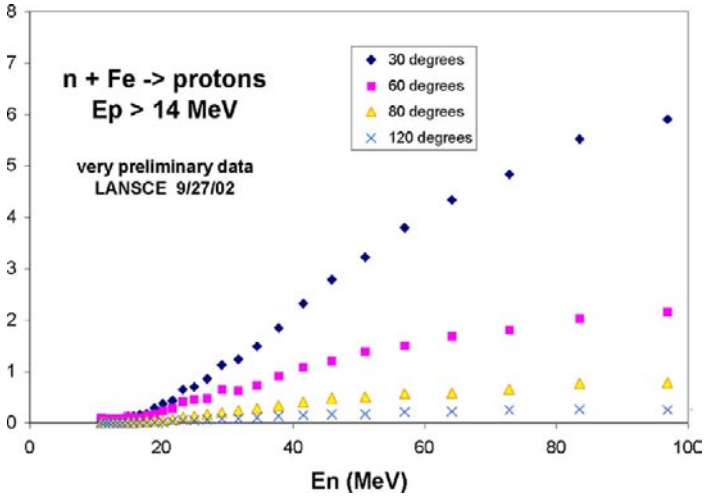

Fig. 4.3-3: Preliminary results for proton emission from neutron reactions with iron.

4.4. Irradiation Effects on Oxide Layer

Objective

The objective of this study was to investigate the effect of proton irradiation on oxide films formed on materials of interest in contact with LBE.

Accomplishments

LBE corrosion experiments were performed in the furnace shown in Fig. 4.4-1. This furnace was made from off-the-shelf 1.5" O.D. SS-304L tubing (ultra high vacuum tubing). Heating was supplied by a 700-W band heater (1-inch x 2-inch-diam.) and regulated to within 3°C of the setpoint with an Omega controller and a type-K thermocouple. To avoid excessive oxidation of the LBE melt, the furnace was continuously flushed with argon during the course of the tests. The sample to be tested in the furnace assembly was welded to the end of a piece of SS-304 tubing. At the opposite end the tubing was welded to an electrical feed, electrically isolating the sample from the SS furnace.

The flux of the incident proton beam had a Gaussian distribution of σ ~ 0.7 cm. The energy of this particle beam was 800 MeV. The pulsed beam was characterized by a gate length (macropulse) of 100 ms, a macropulse repetition rate of 100 Hz, and a fixed peak current of 16 μA (Fig. 4.4-1). These duty cycle parameters yielded an average proton beam current of 63 nA. Both HT-9 and SS-316L were tested in the WNR experiments. These samples were prepared by polishing and sequentially cleaning in acetone, ethanol, and DI water. This was followed by oxidation in moist air at 800°C for 48 hrs for HT-9 and 70 hrs. for SS-316L. Following grinding, cleaning, and preoxidation, the samples were subsequently immersed in LBE for up to 72 hrs.

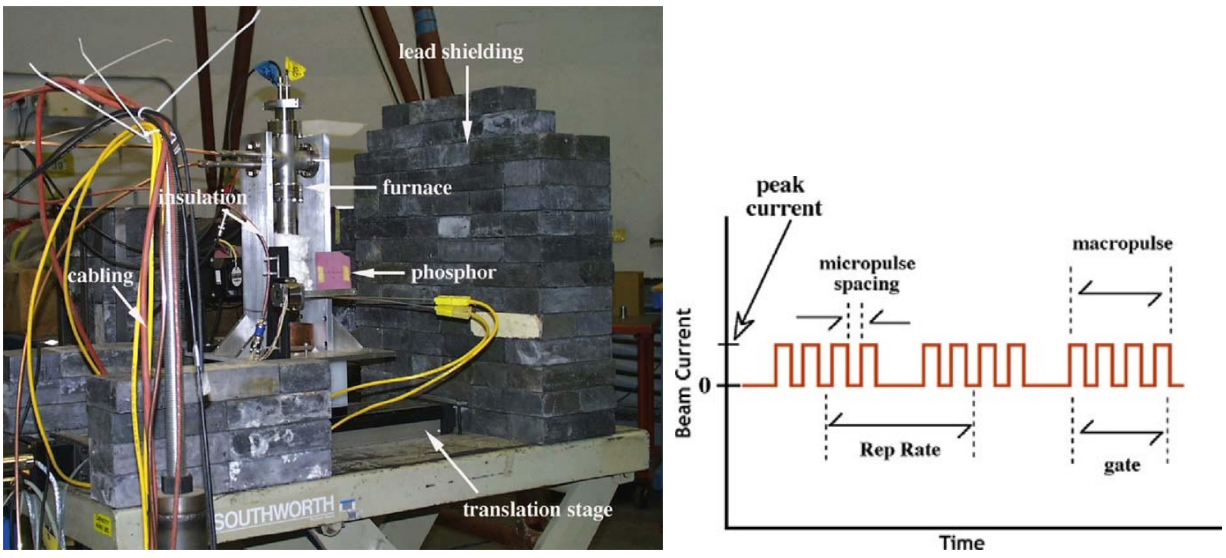

Fig. 4.4-1: Photo of the furnace at WNR used for in-beam experiments and a diagram depicting the proton beam current time relationships.

Impedance data (R_{ox}) for an HT-9 sample as a function of immersion time in the WNR furnace is presented in Fig. 4.4-2. Prior to irradiation with protons, R_{ox} increased steadily and appeared to be nearing a plateau value of ~10^4 W·cm^2. After 247 min of immersion, the proton beam was turned. Correspondingly, R_{ox} was observed to decrease. After ~28 minutes of irradiation, the proton beam was turned off. For ~60˚minutes after the proton beam was turned off, R_{ox} continued to decrease at a rate similar to that observed during irradiation. After this period, both high and low values of R_{ox} were observed indicating the sample impedance was unstable.

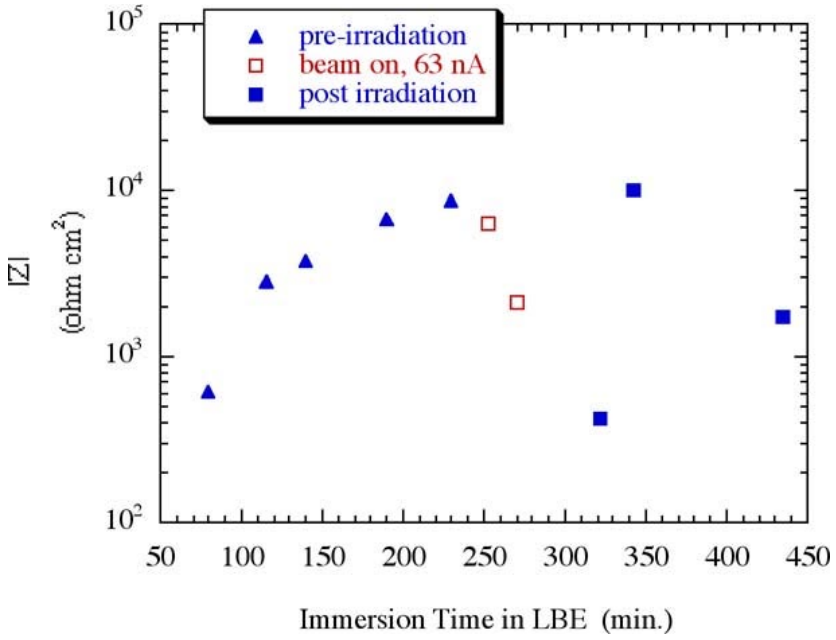

Fig. 4-4-3: Oxide impedance as a function of immersion time in LBE.

Conclusions:

While we are not prepared to speculate as to why the experimental trends were observed during/after proton irradiation, the behavior was reproducible. Therefore, it appears for these experimental conditions, mixed radiation fields may adversely influence oxide properties. A full analysis of the data is planned for FY03.

For additional information contact Scott Lillard (LANL) at lillard@lanl.gov .

5. HIGH-ENERGY PHYSICS

Objective:
The objective include updating the MCNPX code to improve the modeling capabilities relevant to transmutation. The scope of the MCNPX work also includes user-support. Likewise, to support the need of improved predictions for transmutation, cross-section evaluations are performed starting with the major needs. FY02 objectives were to complete the Pu-239 fission cross-section and lead inelastic scattering cross-section evaluations. Both MCNPX and cross-section evaluation tasks are long-term tasks to support the transmutation science activities throughout the 5-year research program.

Highlights:
The following are the major highlights in FY02 for the high-energy physics activities:

- ¥ Two MCNPX revisions were released to RSICC, the latest one is version 2.4.0.
- ¥ A number of MCNPX courses were taught at the universities and International research centers.
- ¥ Mix-and-Match capability and Light-Ion Recoil models are incorporated into the latest MCNPX version.
- ¥ A new inelastic scattering cross-section evaluation is developed for lead, which may result in a 2.5% difference in the reactivity coefficient predictions for LBE-cooled transmuters.
- ¥ A new evaluation of 239-Pu and 238-U fission cross-sections were developed which are in good agreement with the recent data.
- • Improvements of a modified version of the CEM2k code to describe fission fragment production were completed, and our CEM2k+GEM2 code can now be used with confidence to predict fission neutrons for the LA150 actinide libraries.

Major Tasks:
The following are the major tasks summarized in the subsequent sections

5.1. MCNPX Code Development

Objective:
The FY02 objectives were to release versions 2.3.0 and 2.3.4 to Radiation Safety Information Computational Center (RSICC), to add the Mix-and Match Capability, the Light-Ion Recoil Model and The Cougnon-Schmidt model to the code, and to provide user support via MCNPX courses.

Accomplishments:
Code Releases
MCNPX version 2.3.0 was released to the in December 2001 to RSICC. New code features include the capability to use proton and photonuclear libraries, as well as the secondary particle-biasing variance-reduction technique needed to efficiently model high-energy hadronic showers. AAA applications have special problems in simulating these since the low-energy neutrons produced in the shower will greatly multiply in the transmuter blanket. Improvements were also made to mesh and radiography-tally capabilities as well as energy deposition tallies. The full set of 150-MeV neutron, proton, and photonuclear libraries now available was also included in the code release, along with an updated User s Guide.

After a series of test versions (2.3.d through 2.3k), in Summer of 2002, MCNPX version 2.4.0 was formally released to RSICC, and several useful capabilities in the next version of the code were added. This version fully updates MCNPX to MCNP4C, and also rewrites the entire code in Fortran-90. An automated build system was released with the code, which uses the 'config' utility to query the hardware directly as to what operating system, compiler, and run-time libraries are available. The build system eliminates the need to issue separate versions of the code for different platforms. An updated MCNPX 2.4.0 User's Manual was also prepared, and the notice of the 2.4.0 code release is was posted in the October 2002 RSICC newsletter.

International Collaborations
In November 2002, we met with staff from Saclay to discuss implementation of the Cugnon Intranuclear Cascade model and the Schmidt evaporation model into MCNPX. A draft Memorandum of Understanding was produced that outlines the responsibilities of all parties and how updates to and distributions of the software will be handled. We received the Cugnon INC and Schmidt evaporation models from our collaborators at Saclay in June 2002. These are currently being implemented into MCNPX. Because of the delays in receiving the model, this task was not completed in FY02.

Classes Taught
The following MCNPX classes were taught during the year:
- University of Las Vegas, Nevada (January 14—18). The class included 14 UNLV and 2 Idaho Accelerator Center collaborators. This was a beginning-level class, especially suited to students funded under the AAA University Program.
- Tokyo, Japan (February 18—22). This class attracted students from the JAERI high-energy physics facility.

- ¥ Knoxville Tennessee. This class was taught primarily for the benefit of the ORNL accelerator community. ORNL has also finalized the inclusion of the latest version of the CEM code in MCNPX,
- ¥ Santa Fe Community College (July) with 15 registered students.
- ¥ San Diego in September with 12 students.
- ¥ A class co-sponsored with SCK-CEN in Belgium was announced for the week of November 18th. This class will be co-sponsored with NEA, RSICC and KTH in Sweden.

As of October 1st, there are 911 registered MCNPX beta testers at 201 institutions internationally.

Mix-and-Match Capability

The 'Mix and Match' capability essentially has two parts: (1) the ability to designate different libraries for the various particles (isotope mixing), and (2) the ability to use different energy limits between nuclear data table and physics models (energy matching). The isotope-mixing problem was solved, and the user can now choose any library desired for neutron, proton and photonuclear interactions. For example, the user can designate natural carbon for neutrons, and carbon-12 for protons. MCNPX 2.5.a also has the latest CEM2k implementation, which includes a complete energy match solution for the photonuclear component. Thus, different transition energy limits may be specified for each isotope chosen for photonuclear reactions in the same problem. A photonuclear physics model is also included for all isotopes. Previously, we were limited to the 12 available nuclear data libraries. Based on the photonuclear implementation of energy matching, the same capability was added for neutrons in version 2.5.a.

Light-Ion Recoil Model

Light ion recoil was added to the MCNPX code so that light residual nuclei are treated as fully transportable particles. A Fermi Gas treatment was also implemented for protons, which improves the accuracy of energy deposition calculations in light materials. In previous versions of the code, these light ion recoils were not transported, and their energies were deposited locally.

Conclusions:

Considerable improvements were made to the MCNPX code in FY02. The code s capabilities for reliable prediction of transmutation are improving continuously. The code has a large user group world-wide and the number of users are increasing continuously. The classes taught during the year benefited International users as well as domestic University users.

For additional information contact Laurie Waters (LANL) at lsw@lanl.gov .

5.2. Lead Inelastic Scattering Cross-Section Evaluation

Objective:
Deficiencies in the existing LA150 lead (Pb) inelastic evaluation were noted by Obninsk researchers (Ignatyuk *et al.*) and ANL researchers (Finck *et al.*), who were concerned about the impact this would have on reactivity (k_{eff}) predictions. In FY01, we concluded that the ENDF LA150 evaluation does need improvement below 5 MeV. The FY02 objective was to provide a new evaluation that improves the predictions in this energy range.

Accomplishments:
We completed our new evaluation of inelastic scattering to the first excited state in Pb at 2.61 MeV. Accurate inelastic scattering in Pb is important for predictions of ATW criticality in a Pb-Bi cooled transmuter, and our new evaluation, which reduces the previous ENDF cross-section by ~0.5 barns at 3.5 MeV, should provide a significant improvement.

Experimental data on inelastic scattering (MT51 in ENDF parlance) to the first excited state (2.61 MeV) below 5 MeV neutron energy are limited. A more recent measurement (1994) from Los Alamos by Vonach also provides valuable information. The Vonach experiment measured the gamma-ray decay of the 2.61-MeV state, and included inelastic cross-section to the 2.61-MeV state, but also to higher states that gamma-ray decay to the 2.61-MeV state. By restricting ourselves to energies below 3.75 MeV, we only have to consider the first three excited states. At an energy of 3.2 MeV, the Vonach data are identical to the inelastic MT51 cross-section. Between 3.2 and 3.75 MeV, we can infer the MT51 cross-section by subtracting the inelastic cross-sections to the second and third excited states from the Vonach (n,n'γ) data.

We have also undertaken nuclear model calculations to guide our evaluation of this cross-section. These include compound nucleus Hauser-Feshbach calculations using the GNASH code, as well as direct reaction coupled-channel calculations using the ECIS optical model code based on the coupling scheme developed by Young. Based on the aforementioned experimental data and the nuclear reaction model calculations, we evaluated the MT51 inelastic scattering cross-section as shown by the bold line in Fig. 5.2-1. The modification is rather large, with the inelastic cross-section being about 0.5 barns smaller at its peak. For comparison, we also show the recent JENDL3.2 evaluation, which peaks at a similar value but has a somewhat unphysical behavior at higher energies. Since the total neutron cross-section is known rather precisely from experiments, and the partial cross-sections must sum to the known total value, we have increased the neutron elastic cross-section accordingly in the 2.6—5-MeV region. The maximum percentage increase in the elastic scattering cross-section is 8%, at 3.5˚MeV.

Conclusions:
Even though it is not tested on a realistic AAA problem yet, the improvements on the lead inelastic scattering cross-sections are expected to have considerable impact on the accuracy of prediction in LBE cooled systems. To cite an example, ECN staff performing MCNPX calculations for ATW systems, were interested in receiving our new AAA-funded ^{208}Pb ENDF evaluation to test the sensitivity of our inelastic scattering upgrade on k_{eff}. Their preliminary work suggests ~2.5% effect, which is considered large.

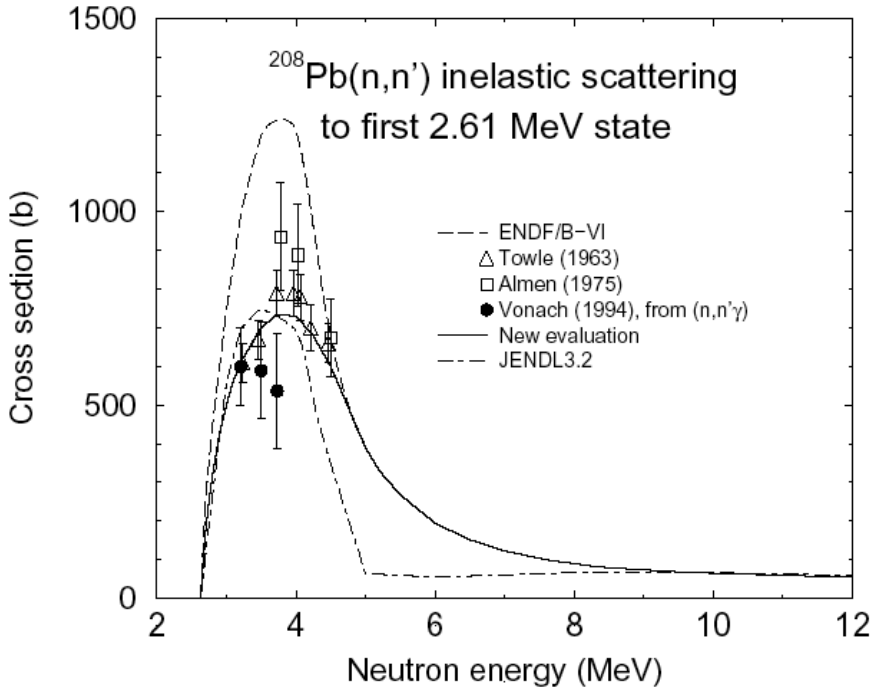

Fig. 5.2-1: ^{208}Pb inelastic scattering cross-section evaluations.

For additional information contact Mark Chadwick (LANL) at mchadwick@lanl.gov .

5.3. Pu-239 and U-238 Fission Cross-Section Evaluations

Objective:
The objective was to provide an improved evaluation of the Pu-239 and U-238 isotopes to increase the accuracy of the transmutation studies. This is the beginning of a series of tasks for cross-section evaluation improvements on transuranic isotopes.

Accomplishments:
We have completed the ENDF formatting of our new ^{239}Pu and ^{238}U evaluations. This required merging the prior ENDF/B-VI file up to 20 MeV incident energy with new sections/subsections obtained up to 150 MeV. Some codes developed for the creation of the LA150 library were used for our present purpose. However, the previous evaluations concerned only non-fissile nuclei, and the associated codes were therefore not intended to be used for fissile ones. As part of our current work, we have developed various additional tools (mostly in the Perl programming language) to deal with this particular situation and others. In doing this ENDF formatting, we went through various steps regarding the physics of the final evaluation. First of all, we modified the calculated (n,tot) cross section to better agree with available accurate experimental total cross-section data (from Lisowski at LANSCE). We then had to renormalize the elastic subsection (MF3 MT2 in ENDF parlance) in the ENDF file to reflect the change in the total cross section (MF3 MT1). Because of the presence of fission, no recoils were included (since the fission fragments dominate recoil energy deposition). We performed a regridding of the entire energy grid above 20˚MeV and up to 150 MeV. The elastic scattering angular distribution (MF=4,MT=2) was taken directly from our ECIS optical model calculations. The energy-angle distributions for the reaction products were taken from the GNASH output. Finally, the neutrons emitted from the fission fragments were calculated with the CEM/Furihata code.

The aforementioned evaluations for neutrons on ^{239}Pu and ^{238}U up to 150 MeV were based on GNASH nuclear model calculations as well as CEM calculations to obtain the fission neutron spectra information. The ^{238}U nucleus is valuable to study because of the larger amount of experimental data available, compared to other actinides. The LANL total cross-section data (Abfalterer, Dietrich et all, funded by APT, and Lisowski), together with absorption and elastic scattering data, enabled us to develop a new relativistic high-energy optical potential for ^{238}U and ^{239}Pu. This was important for allowing us to model and evaluate (n,fission) as well as (n,xn) neutron production cross sections.

Figure 5.3-1 shows our GNASH-calculated fission cross-section compared to recent measurements. Agreement is seen to be good, though at the highest energies the fission cross-section over-predicts the data when the default optical-model reaction cross-section is used. However, the high-energy behavior of the neutron-reaction cross-section is not well know. If the reaction cross-section is decreased to a somewhat smaller value in the 90—150MeV region, as shown by the dashed line in Fig. 5.3-2, we obtain agreement with the Lisowski fission data (dashed line in Fig.˚5.3-2). Further work is needed to determine which reaction cross-section is best to use. We have had discussions with Lisowski on the systematic uncertainties associated with the recently released high-energy Lisowski fission data (2001). This is needed so we can combine these data with Scherbakov's new St. Petersburg data in a covariance analysis of the ^{239}Pu(n,f) cross-section up to 150 MeV.

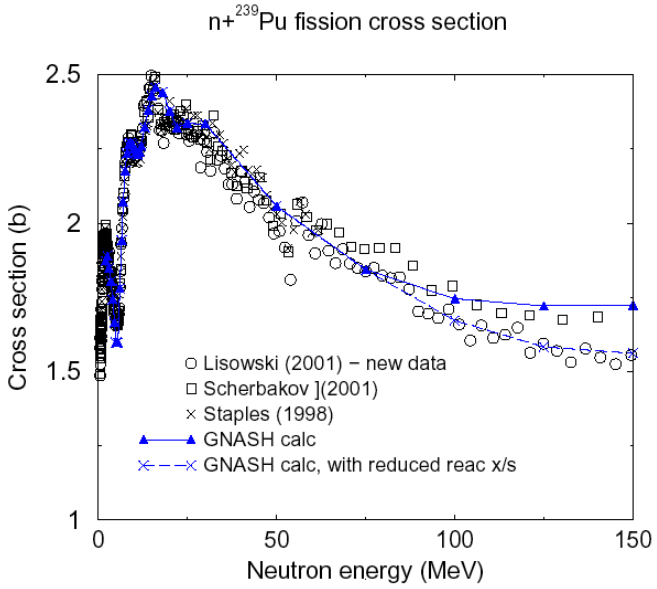

Fig 5.3-3: GNASH-calculated fission cross-section compared to recent measurements.

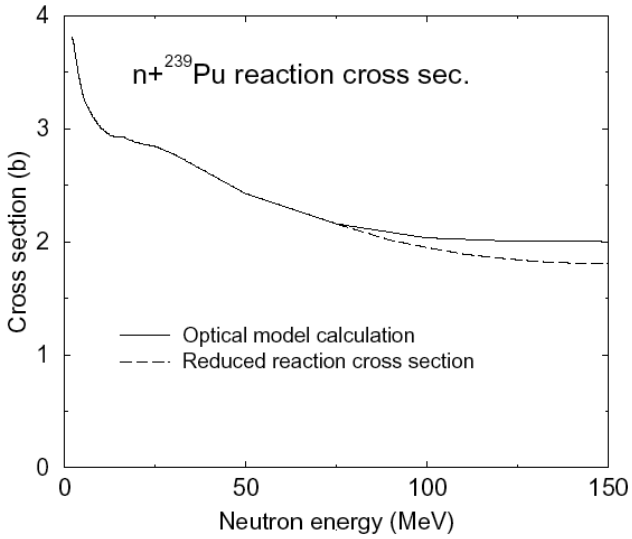

Fig. 5.3-4: Comparison to Lisowski s fission data.

Conclusions:
The new evaluations of 239-Pu show improved agreement with the available data. Additional checking and validation work for these new actinide LA150 high-energy evaluations will include: (1) Performance in MCNPX; (2) Comparisons with some recent Russian cross-section work that supports ADS applications in Europe, Japan, and Russia; and (3) Comparison with thin- and thick-target measurements where available.

For additional information contact Mark Chadwick (LANL) at mchadwick@lanl.gov or Patrick Talou (LANL) ptalou@lanl.gov .

5.4. CEM-2K Code Development

Objective:
The objective is to develop a modified version of CEM2k code to describe fission fragment production with the subsequent evaporation of neutrons and other particles.

Accomplishment:
To describe fission and light-fragment (heavier than ^{4}He) production, the CEM2k code has been merged with the GEM2 code of Furihata, which contains evaporation of up to 66 different particles and a fission model based on Furihata's modification of the Rutherford-Appleton fission model by Atchison from LAHET. We tested this modification of our code on fission cross sections, mass distributions and yields of fission fragments for all reactions measured recently at GSI (Gesellschaft f r Schwerionenforschung in Darmstadt, Germany) and several more reactions measured earlier at other laboratories. We found that a number of modifications have to be made in the Furihata code, GEM2, to solve many technical problems we met when simulating evaporation from compound nuclei with a very high excitation energy, or when calculating evaporation of particles from light nuclei. The fission part of the Furihata code had also to be improved to be able to obtain correct fission cross-sections both for actinides and pre-actinides.

To better describe complex particle emission at the pre-equilibrium stage of reactions, we improved the calculation of the probability of several excitons to coalescence into a complex particle that can be emitted along with nucleons during the equilibration process. All these improvements allowed us to better compute both fission and spallation reactions and to obtain a better agreement with measured data in comparison with other modern codes used by the applied nuclear physics community.

An example of our fission results is compared in Fig. 5.4-1 for the yield of all measured isotopes from p(100 MeV) + ^{238}U with experimental data from Titarenko[4] and with results to predictions by the NASA phenomenological model YIELDX of Sliberberg, Tsao, and Barghouty, and to the LANL phenomenological code CYF by Wahl. We see that our new CEM2k+GEM2 code describes these measurements so well that our results almost coincide with the data covering most of the data points in the Fig. 5.4-2, while both the phenomenological codes fail here. Our CEM2k+GEM2 code can now be used with confidence to predict fission neutrons for the LA150 actinide libraries.

Another example of our results, for a spallation reaction of interest to AAA, is shown in Fig. 5.4-2, where we compare the CEM2k+GEM2 predictions with the recent GSI measurement of the reaction p (1 GeV) + Fe56. We also compare our calculations to: results obtained from the last version of the intranuclear cascade model by Cugnon coupled with the Schmidt'd evaporation/fission model (INCL) incorporated recently into LAHET and MCNPX; and results from the ISABEL code, also used by both LAHET and MCNPX transport codes. Note that the INCL (Cugnon + Schmidt) code was developed and the GSI measurement was done for the HINDAS project of the European transmutation of nuclear wastes project. One can see that our new CEM2k+GEM2 code describes these data much better than the new code by Cugnon+Schmidt, and better than ISABEL. Similar results were obtained for all other reactions measured so far at GSI.

[4] (ITEP, ISTC Report 839B-99, Moscow, 2001)

Conclusions:
The accomplishments presented above show that the new CEM2k+GEM2 code describes these data much better than the new code by Cugnon+Schmidt, and better than ISABEL. Similar results were obtained for all other reactions measured so far at GSI.

For additional information contact Mark Chadwick (LANL) at mchadwick@lanl.gov or Patrick Talou (LANL) ptalou@lanl.gov .

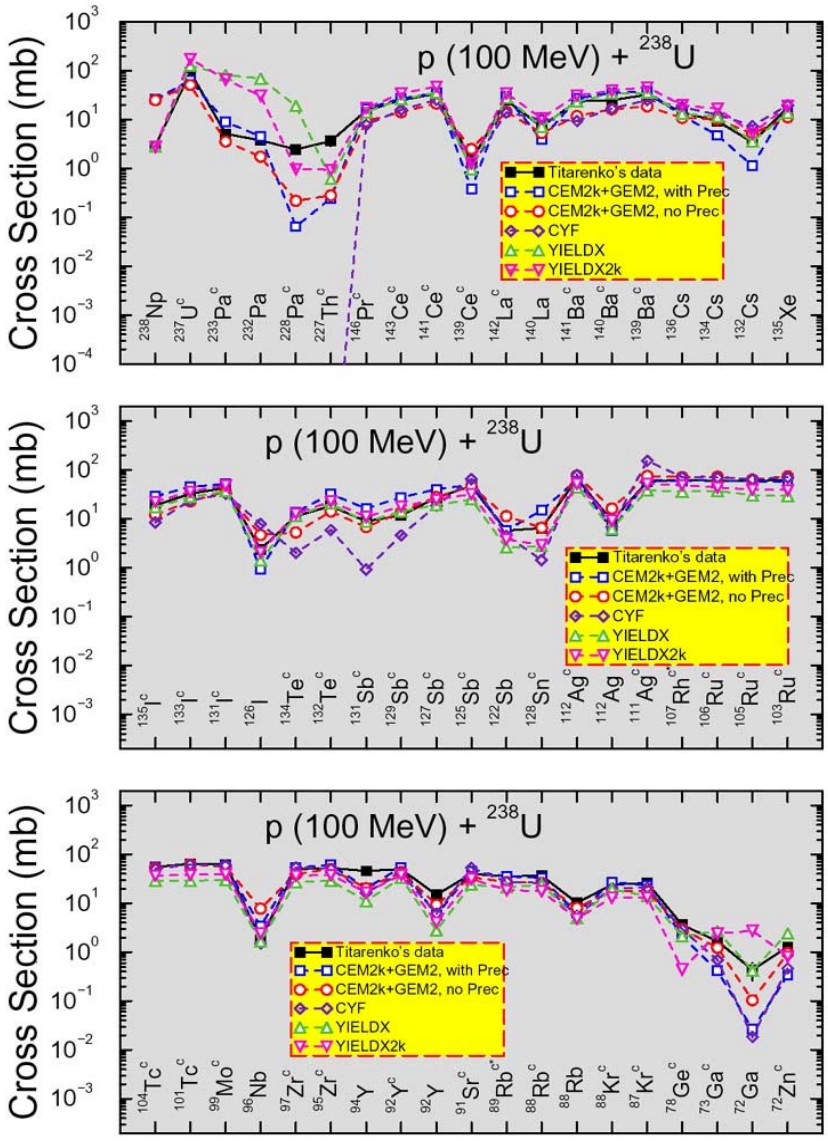

Fig. 5.4-1: Yield of all measured isotopes from p(100 MeV) + ^{238}U

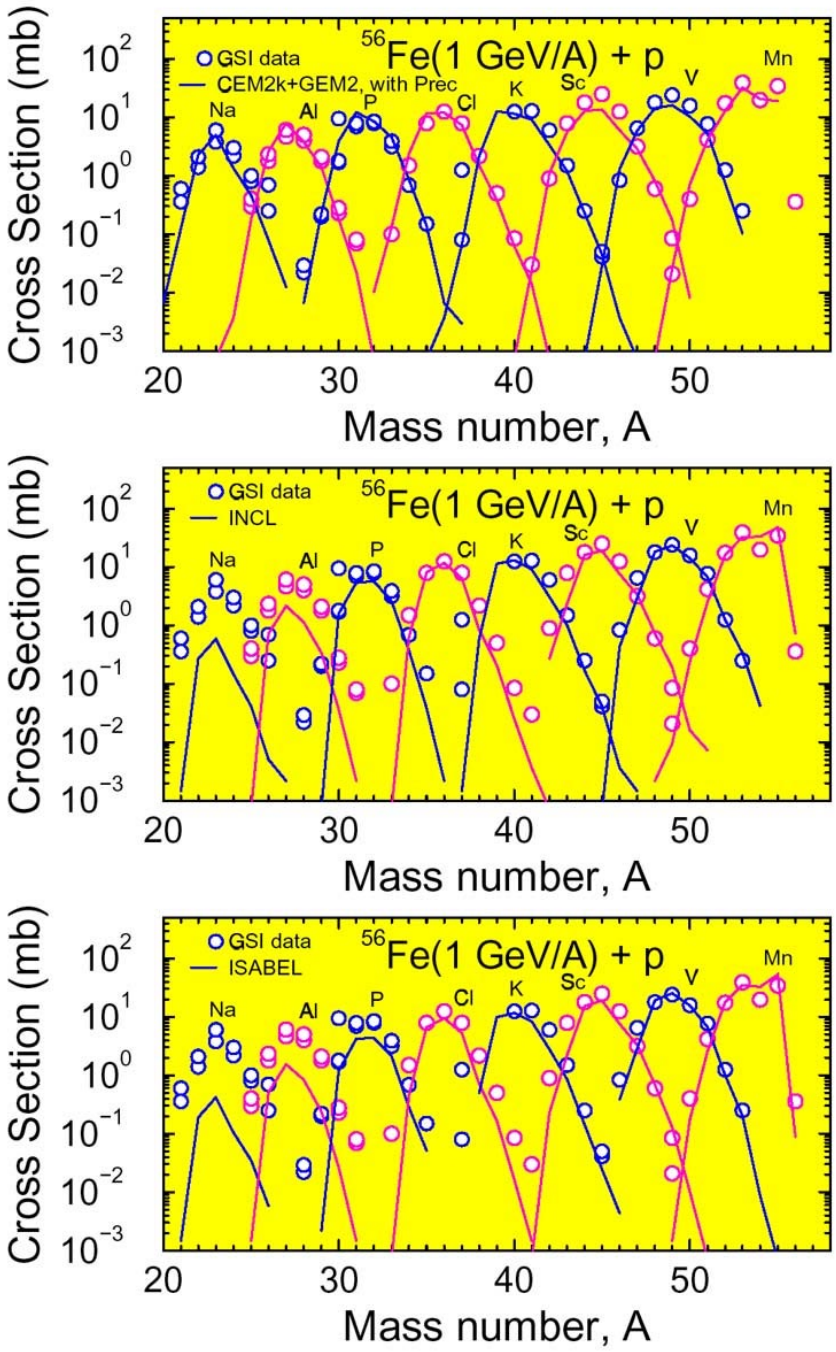

Fig. 5.4-2: Comparison of the CEM2k+GEM2 predictions with the recent GSI measurement of the reaction p (1 GeV) + ^{56}Fe

6. INTERNATIONAL SUPPORT

Objective

The objective of these activities is to provide technical support to International projects that are of interest to the AAA program. The main scope was to provide engineering and analysis support to the MEGAPIE project (PSI, Switzerland). Technical review support the MYRRHA project (SCK-CEN, Belgium) and import of the ISTC target from Russia to U.S.A. also were within the FY02 scope.

Highlights

The following are the FY02 highlights for the International Support tasks:

- Under a very aggressive schedule, MEGAPIE project is progressing well. LANL contributed to the project by sending Keith Woloshun (for 6 months) and Eric Pitcher (for 3 months) to PSI to work on MEGAPIE tasks.

- LANL participated in the technical design review of the MYRRHA project. The review revealed that another few years worth of research is needed pior to a final design study.

- The International Science and Technology Centre (ISTC) LBE target fabricated by the Institute of Physics and Power Engineering (IPPE) in Obninks, Russia, was delivered to the University of Nevada at Las Vegas (UNLV).

Tasks

The following tasks are further discussed in the next sections:

6.1. MEGAPIE Project Support

Objective:
Per collaboration agreement, engineering and analysis support are provided to the MEGAPIE project by LANL staff stationed at PSI.

MEGAPIE Project Status
In FY02, the MEGAPIE Project has made significant progress toward the goal of irradiation in 2005. A brief summary of major events and milestones for MEGAPIE in FY02 (fourth quarter) is given below.

The target system design was essentially completed (see Fig. 6.1-1). Although there remains a list of details that must be resolved, drawing packages and documentation are now being finalized. A bid solicitation was issued and a vendor tentatively selected. The vendor requires a complete specification of the design by December, 2002 to insure delivery by the end of 2003.

The ancillary system designs are complete. Some documents are still in review. Drawing packages, instrumentation specifications, procurement specifications, and operating procedures, are essentially complete.

The prototype pump and flow meter were fabricated and tested. These tests showed pump performance better than required. Flow meters were operating successfully, but improvements and more testing, with improved instrumentation, are required. No cavitation has been observed even with overpressures as low as 3 mBar.

Initial LISOR tests began, but have been problematic. The first test was stopped because of an amplifier failure, and the second test failed, most likely due to cyclic fatigue, caused by a highly focused beam (2.5 mA/cm^2) that wobbled at too low a frequency (1x14 Hz over a rectangular beam footprint). Material tests will resume in October with new beam parameters. A potentially significant observation is that while the bulk of the T-91 sample remained unwetted by LBE after irradiation, the portion of the sample in the beam-spot was wetted.

Efforts are ongoing to minimize the complexity of the ancillary systems. Most notably, the fill-and-drain system may be replaced with a fill-only system. The LBE would be allowed to freeze inside the target to be drained later in a hot cell. Detailed studies of the LBE expansion after freezing, due to recrystalization of the solid, are being conducted to see if the target can be frozen without breaking the target window. Another possible simplification of ancillary systems is the minimization of the cover gas system. The current system, which includes a decay tank and a sampling capability, could be replaced with a sealed system if it can be shown that the gasses generated during irradiation can be contained at low enough pressure in the available volume.

DOE Accomplishments
MCNPX Model of the MEGAPIE Target
A new MCNPX model of the MEGAPIE target has been developed based on the latest design drawings. The model extends out to the light-water jacket that surrounds the

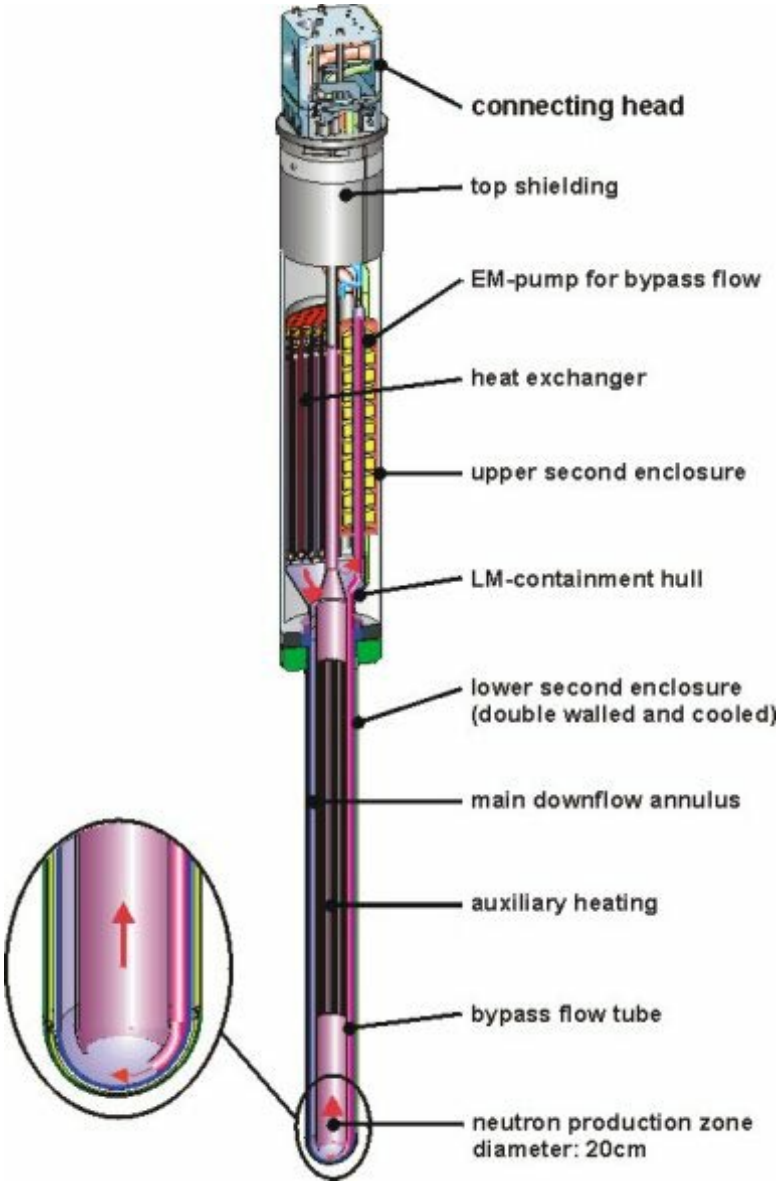

Fig. 6.1-1: MEGAPIE target conceptual layout.

heavy-water moderator tank. Figure 6.1-2 shows a vertical cut through this geometry. The model has high fidelity in faithfully representing the actual geometry of the target and safety hull in the vicinity of proton beam interaction. This includes the bypass flow tube, and target catcher that is designed to protect the safety hull should the LBE target container fail for some reason.

The proton beam profile used in the MCNPX calculations is based on simulations carried out by Urs Rohrer. The x- and y-profiles are assumed to be separable, that is, $P(x,y)^{\circ}={}^{\circ}p(x)^{\circ}q(y)$, where $p(x)$ and $q(y)$ are the y- and x-integrated profiles. Figure 6.1-3 shows his calculated x-y profile and the profile used in the MCNPX calculations. Rohrer s calculations predict a peak current density at the center of the beam of 29.6 $\mu A/cm^2/mA$ of beam current, whereas the profile used in the MCNPX calculations has a peak current density of 30.3 $\mu A/cm^2/mA$. The proton energy used is be 575 MeV.

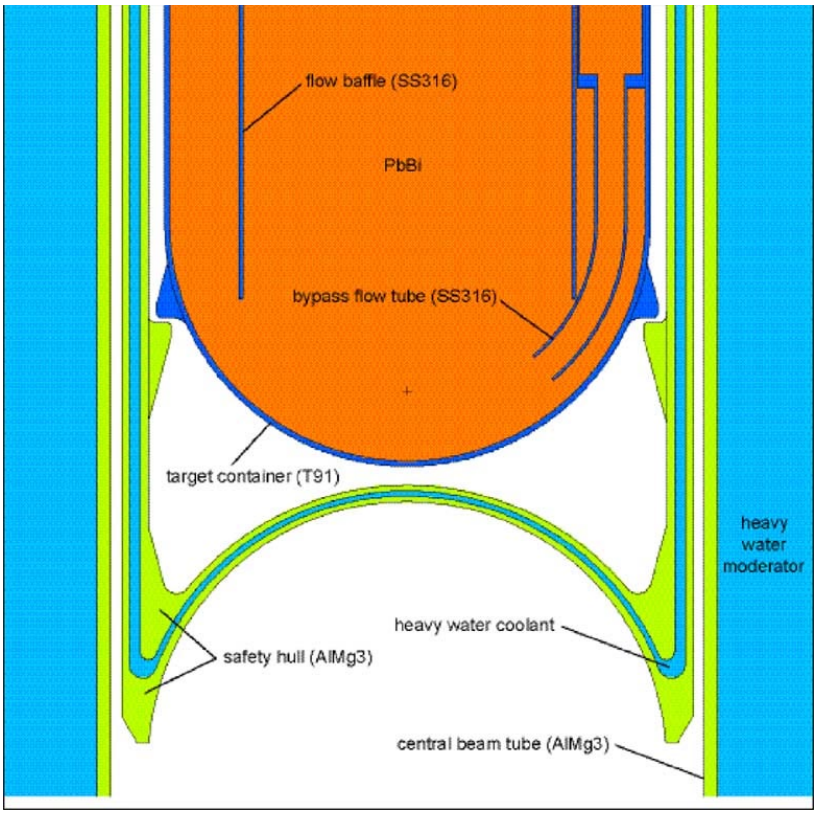

Fig. 6.1-2: Vertical slice through the MCNPX model of the MEGAPIE target.

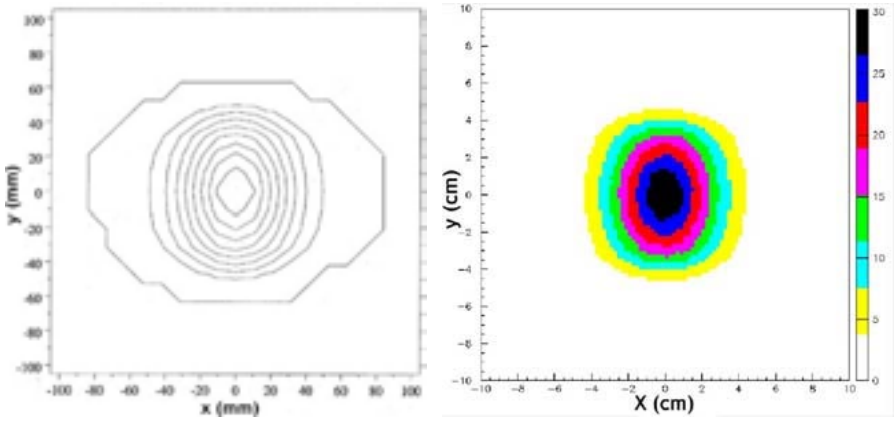

Fig. 6.1-3: MEGAPIE beam spot contours: (a) Rohrer s prediction contour lines are 10% integrals; (b) MCNPX source units on the color bar are μ A/cm^2.

MEGAPIE Fluxes

Proton and neutron fluxes in the MEGAPIE target have been calculated. The proton flux is shown in Fig. 6.1-4. The 575-MeV protons range out after traversing about 27 cm of Pb-Bi. Peak proton flux on the central beam tube is ~3x10^{11} p/cm^2/s. Neutron flux plots are shown in Fig. 6.1-5. The neutron flux is highest in the center of Pb-Bi target, at a depth of ~6 cm from the front face. Peak neutron flux at this point is about 1.1x10^{15} n/cm^2/s. The thermal (<0.625 eV) flux peaks in the heavy water at a distance of about 21 cm from the proton beam centerline, with a peak flux near 1.5x10^{14} n/cm^2/s.

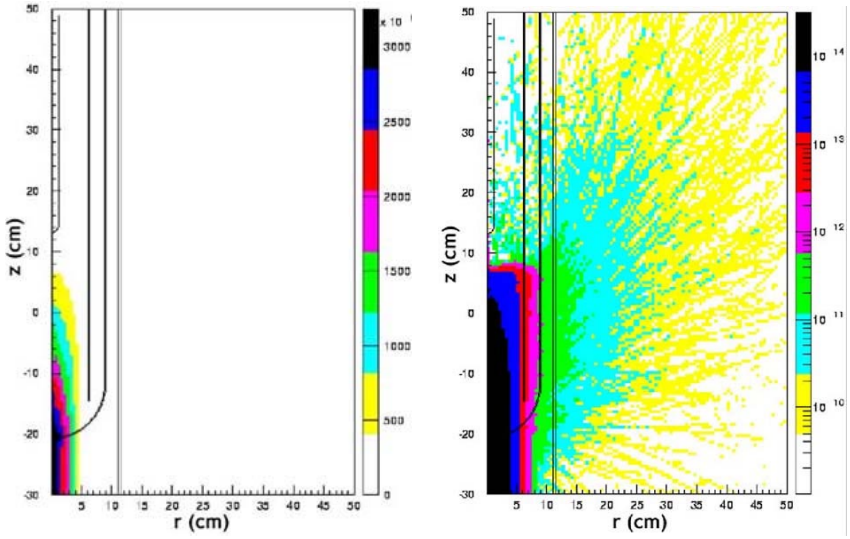

Fig. 6.1-4: Proton flux at 1.74 mA beam current: (a) linear scale; (b) log scale.

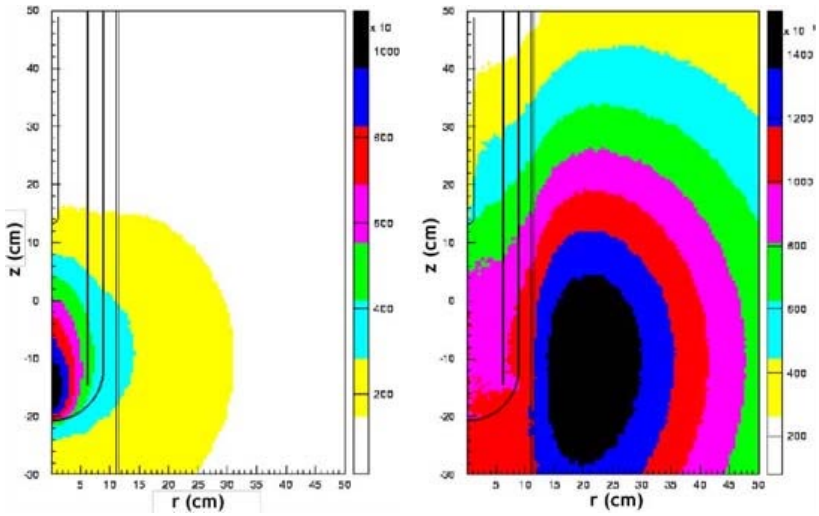

Fig. 6.1-5: Neutron fluxes at 1.74 mA beam current: (a) total flux; (b) thermal flux

Pb-Bi Radionuclide Inventory

The build-up of radionuclides in the Pb-Bi during the anticipated operation of the MEGAPIE target was calculated using the MCNPX and CINDER 90 codes. Spallation-product generation rates and low-energy (<25 MeV) neutron fluxes were calculated by MCNPX, and these data passed to CINDER 90, which was used to calculate time-dependent nuclide inventories during and after a 200-day irradiation at 1.74 mA beam current (8.35 A•h). The activities of some notable radioisotopes, after 6 A•h of operation at 1.74 mA beam current, are listed in Table 6.1-1. The total radioactivity of the Pb-Bi during 200 days of irradiation at 1.74 mA followed by 30 days of cooldown is shown in Fig. 6.1-6. Six A•h of operation produces 5.3 liters of hydrogen and 1.1 liters of helium at standard temperature and pressure (293 K and 0.1013 MPa). After 200 days of continuous operation at 1.74 mA (that is, 8.35 A•h of charge), the volumetric decay heat (*b*+*g*) in the Pb-Bi is calculated to be 0.060 W/cm^3, which gives a total decay power of 4.9 kW within the 82-liter volume of Pb-Bi in the loop.

Radiation Dose to the Diphyl Oil in the MEGAPIE Primary Heat Exchanger

We performed a neutronics analysis of the dose rate to which the THT oil (the working fluid in the secondary loop of the MEGAPIE Pb-Bi cooling system) is subjected during operation. Three sources of radiation exposure were evaluated:

- activated heavy water that cools the safety hull,
- activated Pb-Bi,
- prompt radiation.

Of these sources, the activated Pb-Bi dominates the dose received by the oil. The Pb-Bi activity was divided into two terms: a short-lived component, and a long-lived component. The short-lived component represents short-lived radionuclides that are

Table 6.1-1: Activities of Some Notable Isomers in the Pb-Bi after 6 AÆh of Operation.

Isomer	Half-life (s)	Activity (Ci)
H-3	3.89×10^{8}	310
Ar-41	6.58×10^{3}	0.0088
Kr-79	1.26×10^{5}	69
Kr-83m	6.59×10^{3}	240
Kr-85	3.38×10^{8}	2.0
Kr-85m	1.61×10^{4}	160
Kr-87	4.58×10^{3}	140
Xe-127	3.15×10^{6}	69
Xe-129m	7.68×10^{5}	8.0
Xe-131m	1.03×10^{6}	4.5
Po-210	1.20×10^{7}	5060

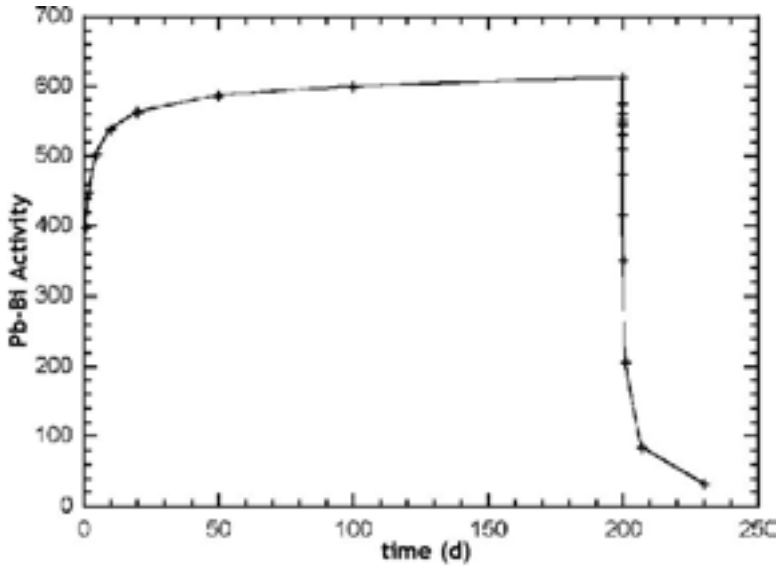

Fig. 6.1-6: Pb-Bi radioactivity during and after a 200-day irradiation at 1.74 mA.

not diluted in the Pb-Bi volume because they decay away before mixing. The activity of the short-lived component varies strongly with position in the loop (e.g., highest at the bottom of the target, lowest in the downcomer region of the target). The long-lived component does not vary significantly with position in the loop.

The depletion code CINDER 90 provides a decay-gamma source term in 25 energy groups at user-specified times during and after irradiation. The source term of the short-lived component is calculated by subtracting the Pb-Bi activity following a long decay period (e.g., 300 s) from the activity after a short (e.g., 10 s) decay period. The short period represents the transit time from the point of Pb-Bi activation (bottom of the target) to the primary heat exchanger, while the long decay period represents the time needed to assure the residual radioactivity is evenly distributed throughout the 82-liter Pb-Bi volume. The two decay gamma source terms (short and long) so derived were then transported in a MCNPX model of the primary heat exchanger. Various permutations of short and long decay periods were used to gauge the sensitivity of the absorbed dose on these parameters. For short decay periods ranging from 3—30 s and long decay periods ranging from 100—1000 s, the calculated absorbed dose to the oil in the heat exchanger varied by —6%/+11% from the mean value of 4.4 W, assuming a beam current of 1.74 mA. When averaged over the 77-kg inventory of oil in the secondary loop, this amounts to an absorbed dose of 0.20 WÆh/g after 6 AÆh of operation.

Oil-LBE Interaction Experiments

A set of experiments was conducted to study an oil-LBE interaction that would result in the event of a heat exchanger leak. Specifically of interest are the gas generation rates and the pressures that will result, possibly leading to more serious mechanical failures. Oil at nominally 150…C and at a pressure greater than the LBE pressure in the target, would leak into the nominally 300…C, with a 350…C peak temperature.

A control experiment was conducted first, heating only the oil up to 350…C and holding for several hours with a slight Ar overpressure. Cover-gas pressure was measured as a function on time and temperature. The cover gas pressure was consistent with the sum of the Ar overpressure and the vapor pressure expected from the suppliers vapor pressure curve. The test was then repeated with both oil and LBE in the autoclave. The result was the same, indicating no oil-LBE interaction. A slight net pressure rise after the system has returned to room temperature indicates that there may be a small amount of noncondensible gas generation. Since the time scale for cooling the target following an accident of this sort is within a few hours, this gas generation will not contribute to any pressure buildup that might compound the accident. Additional tests are being prepared to collect and analyze gas byproducts.

TRAC Model

A TRAC model of the MEGAPIE 3-loop system is being set up to evaluate the system transient performance during operation in SINQ as well as during reduced power tests in the integral test stand. This modeling effort began in the last weeks of this fiscal year and will be continued into FY03.

At this time, a partial model of the LBE side of MEGAPIE is operational, with beam heating and transient analysis capability. Heat dump is to a simplified secondary system. This TRAC model will follow as closely as possible the RELAP5 model developed by Ansaldo

for the heat removal system design basis. The TRAC model will be used to evaluate the steady state and transient test conditions for the integral testing, and for the development of the controls system.

Integral Test Stand

A major activity in FY03 will be the preparation of the integral test stand for out-of-beam testing. We are working with the PSI team to define the test matrix and a heater configuration to simulate beam heating at reduced power. These heater tests will be used to establish the transient response of MEGAPIE as an aid in development of the control system. The current heater concept a dummy outer target container equipped with electrical heaters (estimated 200 kW) will replace the target window during these integral tests. Commercially available cartridge heaters could provide about 200 kW, 1/3 of the thermal operating load of MEGAPIE. Details of the heater selection, mounting, variable power supply, and test matrix are being resolved at this time.

Absorber Tests

Tests of the hydrogen absorbers over the oil and LBE cover gases are now in the planning and analysis stage. In the case of the oil system, the hydrogen produced by radiolysis is about 3 liters (STP), so proper absorber operation is essential to controlling the system pressure. In the LBE cover gas, hydrogen must be absorbed to keep the pressure low and minimize the number of dumps to the decay tank. However, the configuration of the absorber is constrained by the space available. The resulting arrangement of absorber must be tested. The design of these tests is now underway.

Material Data

LANL provided irradiated and unirradiated SS-316L material property data as the baseline data for MEGAPIE. These data were generated and compiled for the Accelerator Production of Tritium Project, representing Chapter 3 of the APT Materials Handbook.

Oxygen Sensor Design

LANL provided to MEGAPIE the detail design drawings of the oxygen sensors in use on the DELTA loop. These sensors may be used on the MEGAPIE integral test stand, and in the actual MEGAPIE test.

Conclusions:

Staff from LANL provided considerable technical support to the MEGAPIE project in the areas of physics and target engineering and testing. The experience gained by the LANL staff may be very valuable if the U.S. decides to deploy a LBE target as part of the AAA program.

For additional information contact Keith Woloshun (LANL) at woloshun@lanl.gov or Eric Pitcher (LANL) pitcher@lanl.gov .

6.2. MYRRHA Technical Review

Objective:
MYRRHA project is aimed at building a LBE cooled, accelerator-driven sub-critical test reactor proposed to be built at SCK-CEN in Belgium. A pre-conceptual design for the reactor is completed and SCK-CEN requested an independent review by an International expert group. If realized, the MYRRHA project and the associated research is of considerable interest to the U.S. AAA program. The objective is to participate in the International review group to understand the details of the MYRRHA status.

Accomplishments
Kemal Pasamehmetoglu from the AAA program chaired the design review meeting for MYRRHA to provide recommendations on a path forward to the SCK-CEN management. The existing design of the MYRRHA project was presented, and the main challenges identified by the review committee were as follows:

- Windowless target and the interface stability require additional testing. Hot spot formation and resulting excessive evaporation must also be addressed.
- Remote handling requires additional demonstration, especially fuel manipulations from under the core.
- Materials damage around the target is an issue that must be resolved through an irradiation program.
- The proposed driver fuel is of known type (MOX, with tested enrichments), but the fuel assembly needs to be redesigned (smaller than prototypic MOX assemblies). Also, the spectrum on the fuel will be harder than what was previously tested. Thus, a fuel testing and qualification program is required.
- Finally, corrosion in LBE is an issue that is being worked worldwide.

The MYRRHA staff is aware of these challenges and is working on aggressive R&D tasks to address the issues. The R&D phase of the program is likely to last for another 3-4 years. The guidance committee recommended that MYRRHA should go forward with a dedicated R&D effort and continue the conceptual design, especially in areas where decisions that can impact the design optimization are not ready yet. For instance, a decision on whether to use a LINAC or a cyclotron must be made soon and then the design re-optimized based on that decision. In general, the MYRRHA schedule of 10 years to deployment is very optimistic and must be revised given the additional research that is needed.

Conclusions:
MYRRHA can be of considerable interest to the AAA program, if realized. In the interim, the reaserch conducted in support of MYRRHA can nicely complement the U.S. research, especially for LBE technology. A strong collaboration between the AFCI program and the MYRRHA project is recommended.

For additional information contact Kemal Pasamehmetoglu (LANL) at kop@lanl.gov .

6.3. Import of the IPPE Target

Objective:
The objective of this activity was to import the IPPE target from Russia to United States. Originally the LBE target was built for irradiation in the LANSCE facility. Subsequently, it was decided to deliver the target to UNLV where it will be used as a research loop.

Accomplishments:
The ISTC LBE target built in IPPE (Russia) was delivered to UNLV in June 2002 (see Fig. 6.3-1). LANL engineers participated in the initial inspection of the target upon receipt at UNLV. A meeting of the International Advisory group was held at UNLV to provide an initial set of recommendations to UNLV for target testing. Based on these recommendations, UNLV will develop the final test plan and start testing the target to support the international effort in LBE technology development. With participation of the Russian engineers, the target-cover gas pressure was tested and it was determined that there are no leaks in the target.

Conclusions:
The target is delivered to UNLV where it will be set-up as a research loop in FY03.

Fig. 6.3-1: ISTC target being unloaded at UNLV.

For additional information contact Curtt Ammerman (LANL) at ammerman@lanl.gov .